Draft version April 30, 2025
Typeset using LaTeX **preprint** style in AASTeX631

Linear Thermal Instability of a Condensing Gas-Particle Mixture

Kecheng Stephon Qian[1, *] and Eugene Chiang[1, 2, †]

[1]*Astronomy Department, Theoretical Astrophysics Center, and Center for Integrative Planetary Science, University of California, Berkeley, Berkeley, CA 94720, USA*
[2]*Department of Earth and Planetary Science, University of California, Berkeley, CA 94720, USA*

ABSTRACT

We study the stability of a hot saturated gas coexisting with condensed particles in an optically thin medium. Such a situation may obtain downstream of a shock, at condensation fronts, or in vaporizing impacts. We show that the gas-particle mixture is subject to a thermal instability whereby a region of lower temperature and higher condensate density cools faster to condense faster. If the region of runaway condensation has a sound-crossing time shorter than its cooling time, then it accretes more mass, in gas and particles, from its higher pressure surroundings. Numerical integration of the linearized perturbation equations demonstrates that this radiation-condensation instability can create particle clumps and voids out of a secularly cooling gas. Provided radiation can escape to cool particle overdensities, thermal instability can help assemble chondrite parent bodies out of the vaporized debris of asteroid collisions, and form planetesimals generally.

1. INTRODUCTION

Condensation fronts, where gas condenses into liquid or solid particles, appear in many contexts. In planetary atmospheres, clouds condense out of water vapor (Earth), sulfuric acid (Venus), carbon dioxide (Mars), ammonia (Jupiter), methane (Uranus), and silicates and iron (brown dwarfs and hot Jupiters; for a introduction to the microphysics of clouds, see Pruppacher & Klett 2010). Water vapor and CO freeze out where molecular clouds and protoplanetary disks are sufficiently cold ("snowlines"; Qi et al. 2013; Cieza et al. 2016). Dust of diverse mineralogies condenses from the outflows of evolved stars (Tielens 2022) and catastrophically evaporating rocky planets (Bromley & Chiang 2023).

Collisions between solid bodies are another source of vapor condensates. Meteor impacts have showered the lunar and terrestrial landscapes with silicate spherules condensed from impact vapor plumes (Johnson & Melosh 2012a,b, 2014). Of particular interest here are CB/CH chondritic meteorites which are nearly completely filled with mm-sized, once-liquid metal nodules and silicate chondrules. These melt droplets are thought to be condensed from vaporizing collisions of differentiated asteroids (Choksi et al. 2021, and references therein; see also Stewart et al. 2025). Impact plumes from colliding rocky bodies are special because they present a nearly wholly condensible medium of hot rock and metal vapor, undiluted by inert, non-condensible gases like hydrogen.

How do fresh melt droplets from an explosion agglomerate into CB/CH chondrite parent bodies? The droplets must have been re-collected promptly and efficiently to explain their nearly 100% volume-filling

* e-mail:kq38@berkeley.edu
† e-mail:echiang@astro.berkeley.edu

fractions. A proposed solution to the "Humpty-Dumpty" problem is a radiation-condensation instability (Chiang 2024). The idea is that in a saturated vapor, regions overdense in particle condensates radiatively cool relative to their surroundings, losing pressure and collapsing into smaller volumes. The plume may fragment into cool, dense clumps of particles surrounded by hot, rarefied vapor, analogous to how thermal instability fragments the interstellar medium into multiple phases (Field 1965; Jennings & Li 2021, and references therein). Chiang (2024) investigated potential nonlinear outcomes in a saturated cloud of silicate vapor by modeling collapsing regions as cavitating bubbles.

We seek here to place the hypothesized radiation-condensation instability on firmer ground by seeing if and how it emerges from a linear stability analysis. We consider an initially uniform density medium composed of a wholly condensible, saturated gas and its entrained particle condensates, and ask whether small disturbances to this fluid grow or damp. Working in the optically thin limit where radiation from particles is allowed to escape to infinity, we will indeed find fast-acting instabilities that grow particle overdensities. Our study is the linear counterpart to the nonlinear explorations of Chiang (2024).

Stability analyses usually presume a background equilibrium state to perturb. In Section 2, to define such an equilibrium, we introduce an arbitrary and fixed source of background heating to balance radiative cooling from background particles. This equilibrium is perturbed to derive an analytic dispersion relation for Fourier modes. We work out modal growth rates, and physically interpret mode behaviors. The goal of this analytic section is to develop physical intuition for the radiation-condensation instability, in the hope that some of the behaviors uncovered will be robust against our use of an artificial heating term in the energy equation.

Section 3 solves the linear perturbation equations numerically. After validating our integrator by reproducing our analytic eigenmodes, we conduct experiments that remove the restrictions of our analytic study — in particular, we eliminate background heating and allow the medium to secularly cool by radiation. This time-dependent background is more physically realistic, as secular cooling better describes the evolution of a collisional plume, or the fluid downstream of a shock front. On top of this time-dependent background we introduce linear perturbations and study their growth.

Section 4 summarizes and places the radiation-condensation instability in the context of Field's (1965) thermal instability.

2. LINEAR STABILITY ANALYSIS OF A FIXED BACKGROUND

We assess the linear stability of a gas-particle mixture, where the two species inter-convert through phase changes, and the particles radiate freely to space. We carry out the usual analytic procedure of Fourier analyzing perturbations to a background state. Fourier analysis and the derivation of a wave dispersion relation require that the perturbations vary smoothly in space and time, and that the background be in a time-independent equilibrium (so that the linear algebraic perturbation equations used to derive the dispersion relation have constant coefficients). As mentioned in §1, to construct such an equilibrium, we will need to introduce a background heating term into the energy equation, to balance radiative losses from background particles. This artifice enables us to analytically survey and explore a wide range of physical behaviors, some of which will hopefully still manifest in more realistic set-ups without background heating. We will comment on which effects may be robust and which effects may not be (see §2.5.1 and §2.5.2), and test our assertions against numerical experiments in §3.

The equations governing our fluid mixture are introduced in their most basic form in §2.1. The background equilibrium state is described in §2.2. Linear perturbation equations are derived in §2.3, and solved for eigenfrequencies in §2.4 and eigenmodes in §2.5.

2.1. *Mass, momentum, and energy equations*

Consider a condensible gas mixed with its liquid or solid particle condensates, of total mass density $\rho_{\rm tot} = \rho_{\rm gas} + \rho_{\rm par}$, for gas density $\rho_{\rm gas}$ and particle density $\rho_{\rm par}$. We do not distinguish between solid and liquid phases for the particles. At the time of their formation, chondrules and metal nodules from CB chondrites were at least partially liquid while suspended in space, to attain their observed spherical shapes.

Gas and particles are assumed to be in thermal and chemical equilibrium: on the pressure P vs. temperature T phase diagram, the mixture is assumed to reside on the co-existence curve, such that the gas pressure is always given by the saturation vapor pressure

$$P = P_{\rm sat}(T)\,. \tag{1}$$

For molten "bulk silicate earth" having a composition similar to olivine-rich chondrites,

$$\log_{10}\left(\frac{P_{\rm sat}}{\rm bars}\right) = -30.6757 - \frac{8228.146\ {\rm K}}{T} + 9.3974\log_{10}\left(\frac{T}{\rm K}\right) \tag{2}$$

(Fegley & Schaefer 2012; for vapor pressures of other refractory materials, see Visscher & Fegley 2013; Perez-Becker & Chiang 2013). The vapor behaves as an ideal gas,

$$P = \frac{\rho_{\rm gas} k_{\rm B} T}{\mu m_{\rm H}}\,, \tag{3}$$

so its density also depends on T only,

$$\rho_{\rm gas} = \rho_{\rm sat}(T) = \frac{\mu m_{\rm H}}{k_{\rm B}}\frac{P_{\rm sat}(T)}{T} \tag{4}$$

for Boltzmann constant $k_{\rm B}$, mean molecular weight $\mu \simeq 30$, and atomic hydrogen mass $m_{\rm H}$.

Gas and particles are assumed to be well-coupled dynamically (gas drag stopping times for particles are assumed short), so that the two species move at a common velocity $\mathbf{v}$. The equations of mass and momentum evolution are given by

$$\frac{D\rho_{\rm tot}}{Dt} = -\rho_{\rm tot}\nabla\cdot\mathbf{v} \tag{5}$$

$$\frac{D\rho_{\rm gas}}{Dt} = \frac{d\rho_{\rm sat}}{dT}\frac{DT}{Dt} \tag{6}$$

$$\frac{D\mathbf{v}}{Dt} = -\frac{1}{\rho_{\rm tot}}\nabla P \tag{7}$$

where $D/Dt \equiv \partial/\partial t + (\mathbf{v}\cdot\nabla)$ is the Lagrangian derivative.

Equation (5) is the usual one for mass continuity; the total density of a fluid parcel (of fixed total mass) changes only by changing the parcel's volume, via the velocity divergence $\nabla\cdot\mathbf{v}$. The velocity divergence is absent from the gas continuity equation (6) because we have assumed $\rho_{\rm gas} = \rho_{\rm sat}(T)$; the saturated gas density of a fluid parcel can only change from temperature changes, and not from volume changes per se. It follows that the particle density of a parcel can change from various effects:

$$\frac{D\rho_{\rm par}}{Dt} = \frac{D\rho_{\rm tot}}{Dt} - \frac{D\rho_{\rm gas}}{Dt} = -\rho_{\rm tot}\nabla\cdot\mathbf{v} - \frac{d\rho_{\rm sat}}{dT}\frac{DT}{Dt}$$

$$= -\rho_{\rm par}\nabla\cdot\mathbf{v} - \rho_{\rm gas}\nabla\cdot\mathbf{v} - \frac{d\rho_{\rm sat}}{dT}\frac{DT}{Dt}\,. \tag{8}$$

The first term on the right-hand side of (8) describes how the particle density changes from parcel volume changes at fixed particle mass (no phase changes). The second term describe how gas and particles can inter-convert from parcel volume changes at fixed temperature. The same phenomenon is evident in a piston enclosing vapor and liquid in equilibrium; at fixed temperature, lowering the piston to shrink the enclosed volume converts vapor to liquid while keeping the vapor density and pressure constant (see any thermodynamics textbook; e.g., Figure 10.1 of Kittel & Kroemer 1980). The third term accounts for phase changes from temperature changes.

The momentum eq. (7) describes how the fluid accelerates from gas pressure, with the inertia given by $\rho_{\rm tot}$ for our assumed well-coupled particle-gas mixture. Though the fluid may be orbiting a star, rotational forces and orbital shear are negligible as long as we focus on processes than unfold over timescales much shorter than an orbital period (the timescale over which Coriolis and stellar tidal forces act). Petrologic experiments constrain chondrules to cool over timescales of hours to days (e.g. Desch & Connolly 2002; Hewins et al. 2018), much less than a heliocentric orbital period at the location of the asteroid belt.

The last equation needed to close the system is the energy equation:

$$\rho_{\rm tot}C\frac{DT}{Dt} = -P\nabla\cdot\mathbf{v} + L_{\rm vap}\left(-\rho_{\rm gas}\nabla\cdot\mathbf{v} - \frac{d\rho_{\rm sat}}{dT}\frac{DT}{Dt}\right) - 4\sigma T^4\rho_{\rm par}\kappa_{\rm par} + \mathcal{H} \tag{9}$$

where $C \simeq 3k_{\rm B}/(\mu m_{\rm H}) \simeq 8\times10^6$ erg/g/K is the specific heat of the particle-gas mixture (neglecting the order-unity difference between particle and gas specific heats), $L_{\rm vap} \simeq 3\times10^{10}$ erg/g is the latent heat of vaporization, σ is the Stefan-Boltzmann constant, and $\kappa_{\rm par}$ is a grey opacity (emissive cross-section per unit particle mass) which depends on the particle size distribution. We adopt, for a single particle size $s = 0.1$ cm and internal particle density $\rho_{\rm p} \simeq 3$ g/cm^3, a fiducial $\kappa_{\rm par} = \pi s^2/(4\pi\rho_{\rm p}s^3/3) = 2.5$ cm^2/g.

From left to right on the right-hand side of the energy eq. (9), the temperature of a parcel can change from:

(i) PdV work

(ii) latent heat release from condensation; the parentheses enclose only those terms in $D\rho_{\rm par}/Dt$ that involve phase changes (thus the first term on the right-hand side of eq. 8 does not qualify)

(iii) energy loss from radiation, modeled by assigning to particles a blackbody volume emissivity $j_\nu = B_\nu\rho_{\rm par}\kappa_{\rm par}$ for Planck source function B_ν. Self-absorption is ignored — the background is assumed optically thin, so that all radiation escapes to infinity. Accordingly, the background must be of finite size, limiting our analysis to perturbations of smaller length scale. The factor of 4 arises from integrating the Planck function first over frequency ν (yielding $\sigma T^4/\pi$) and then over all solid angle (yielding 4π).

(iv) a constant heating term $\mathcal{H}$, introduced to balance radiation losses and formally define a background equilibrium.

2.2. *Background equilibrium state*

A heating term $\mathcal{H} > 0$ is needed to define a background equilibrium temperature $T_0 = [\mathcal{H}/(4\sigma\rho_{\rm par,0}\kappa_{\rm par})]^{1/4} > 0$. In all our calculations below, we take $T_0 = 2300$ K as a fiducial. The background equilibrium state (subscript 0) is spatially uniform (T_0 = constant, $P_0 = P_{\rm sat}(T_0)$ = constant, $\rho_{\rm gas,0} = \rho_{\rm sat}(T_0)$ = constant, $\rho_{\rm par,0}$ = constant) and motionless ($\mathbf{v}_0 = \mathbf{0}$). Over the course of this paper, we will experiment with different values for $\rho_{\rm par,0}$, ranging from zero to $0.1\rho_{\rm gas,0}$.

2.3. *Linear perturbation equations*

We now introduce perturbations in the form of one-dimensional plane-parallel waves. For example, for pressure, $P = P_0 + \delta P \exp i(kx - \omega t)$, where δP is the complex wave amplitude (of magnitude $|\delta P| \ll P_0$), k is the real wavenumber (of magnitude 2π divided by the wavelength), x is one-dimensional position, and ω is the complex wave frequency. The complex exponential form of the perturbation is introduced for mathematical convenience; the physical content is contained in the real part of P. If the imaginary part of ω is positive ($\mathrm{Im}(\omega) > 0$), then the wave amplifies exponentially in time, i.e. the fluid is unstable.

We substitute $P = P_0 + \delta P \exp i(kx - \omega t)$, $T = T_0 + \delta T \exp i(kx - \omega t)$, $\mathbf{v} = v_0\hat{\mathbf{x}} + \delta v\hat{\mathbf{x}} \exp i(kx - \omega t)$, etc., into the evolutionary equations (3, 5, 6, 7, and 9; the condition of saturation equilibrium has been folded into equations 6 and 9). After subtracting off the zeroth-order background terms (including the assumed constant $\mathcal{H}$), and keeping only terms linear in perturbed quantities, we arrive at a homogeneous set of algebraic relations (subscript 0 dropped for convenience):

$$-i\omega\,\delta\rho_{\rm tot} = -\,ik\rho_{\rm tot}\,\delta v \tag{10}$$

$$-i\omega\,\delta\rho_{\rm gas} = -\,i\omega\frac{d\rho_{\rm sat}}{dT}\,\delta T \tag{11}$$

$$-i\omega\,\delta v = -\,\frac{ik}{\rho_{\rm tot}}\,\delta P \tag{12}$$

$$\begin{aligned}-i\omega\rho_{\rm tot}C\,\delta T = &-\,ikP\,\delta v - ik\rho_{\rm gas}L_{\rm vap}\,\delta v + i\omega L_{\rm vap}\frac{d\rho_{\rm sat}}{dT}\,\delta T - 4\sigma T^4\kappa_{\rm par}\,\delta\rho_{\rm par}\\ &-\,16\sigma T^3\rho_{\rm par}\kappa_{\rm par}\,\delta T\end{aligned} \tag{13}$$

$$\frac{\delta P}{P} = \frac{\delta\rho_{\rm gas}}{\rho_{\rm gas}} + \frac{\delta T}{T}\,. \tag{14}$$

Note in (13) we have not assumed $|\delta\rho_{\rm par}|/\rho_{\rm par} \ll 1$; only the background terms have been subtracted, and $|\delta T|/T \ll 1$ assumed to keep terms linear in δT. We will be interested in the case where the background is nearly all gas ($\rho_{\rm tot} \simeq \rho_{\rm gas} \gg \rho_{\rm par}$), in which case $\rho_{\rm par}$ may be so small that $|\delta T|/T \ll |\delta\rho_{\rm par}|/\rho_{\rm par}$. Accordingly, for simplicity, we drop the last term of (13) relative to the second-to-last term:

$$-i\omega\left(\rho_{\rm tot}C + L_{\rm vap}\frac{d\rho_{\rm sat}}{dT}\right)\delta T = -ik\left(P + \rho_{\rm gas}L_{\rm vap}\right)\delta v - 4\sigma T^4\kappa_{\rm par}\left(\delta\rho_{\rm tot} - \delta\rho_{\rm gas}\right) \tag{13a}$$

where $(\delta\rho_{\rm tot} - \delta\rho_{\rm gas}) = \delta\rho_{\rm par}$. The dropped term $-16\sigma T^3\rho_{\rm par}\kappa_{\rm par}\delta T$ will be restored in the more accurate numerical experiments of §3.

To re-cap the small parameters: $|\delta T|/T$, $|\delta P|/P$, $|\delta\rho_{\rm gas}|/\rho_{\rm gas} \ll 1$. We have not assumed $|\delta\rho_{\rm par}| \ll \rho_{\rm par}$ or $|\delta v| \ll v$ (the background $v = 0$). There are further restrictions from mass conservation. Since $\rho_{\rm par} + \delta\rho_{\rm par} \geq 0$ and $\rho_{\rm gas} + \delta\rho_{\rm gas} \geq 0$ (no negative masses), the perturbation densities have "floors":

$$\delta\rho_{\rm par} \geq -\rho_{\rm par} \tag{15a}$$

$$\delta\rho_{\rm gas} \geq -\rho_{\rm gas}\,. \tag{15b}$$

Furthermore, the contribution to $\delta\rho_{\rm par}$ from phase changes alone (i.e. not counting the contribution from particle transport) must be $\leq \rho_{\rm gas}$, as one cannot condense more than what is available in background gas. Likewise $\delta\rho_{\rm gas}$ from phase changes alone must be $\leq \rho_{\rm par}$. Thus there are also "ceilings":

$$\delta\rho_{\text{par, phase change only}} \leq \rho_{\text{gas}} \tag{16a}$$

$$\delta\rho_{\text{gas, phase change only}} \leq \rho_{\text{par}} \, . \tag{16b}$$

Analytically (this section 2), perturbations $\delta\rho_{\text{par}}$ and $\delta\rho_{\text{gas}}$ may always be scaled small enough to stay safely within the bounds (15)–(16), as required by Fourier analysis (where all derivatives are continuous). In our numerical experiments (§3), we will occasionally and by design hit up against the bounds, and enforce them manually.

In matrix form, our simplified linear perturbation equations are:

$$\begin{bmatrix} \omega & 0 & -k\rho_{\text{tot}} & 0 & 0 \\ 0 & \omega & 0 & -\omega(d\rho_{\text{sat}}/dT) & 0 \\ 0 & 0 & \omega & 0 & -(k/\rho_{\text{tot}}) \\ 4\sigma T^4\kappa_{\text{par}} & -4\sigma T^4\kappa_{\text{par}} & ik(P+\rho_{\text{gas}}L_{\text{vap}}) & -i\omega\left[\rho_{\text{tot}}C + L_{\text{vap}}(d\rho_{\text{sat}}/dT)\right] & 0 \\ 0 & -1/\rho_{\text{gas}} & 0 & -1/T & 1/P \end{bmatrix} \begin{bmatrix} \delta\rho_{\text{tot}} \\ \delta\rho_{\text{gas}} \\ \delta v \\ \delta T \\ \delta P \end{bmatrix} = \mathbf{0}. \tag{17}$$

2.4. *Dispersion relation and eigenfrequencies*

Setting the determinant of the 5×5 matrix in (17) equal to 0 gives the dispersion relation:

$$(1+\ell a)\,\omega^3 - ia\omega_{\text{T}}\,\omega^2 - (1+a)(b+\ell)c^2k^2\,\omega + i(1+a)\omega_{\text{T}}c^2k^2 = 0 \tag{18}$$

where we have defined a frequency

$$\omega_T \equiv \frac{4\sigma T^4\kappa_{\text{par}}}{CT} \simeq 0.8\left(\frac{T}{2300\,\text{K}}\right)^3\left(\frac{\kappa_{\text{par}}}{2.5\,\text{cm}^2/\text{g}}\right)\text{s}^{-1}\,, \tag{19}$$

an isothermal sound speed

$$c \equiv \sqrt{P/\rho} \simeq 0.8\left(\frac{T}{2300\,\text{K}}\right)^{1/2}\text{km/s}\,, \tag{20}$$

and dimensionless constants

$$a \equiv \frac{d\ln\rho_{\text{sat}}}{d\ln T} = \frac{8228.146\,\text{K}}{T\log_{10}e} - 1 + 9.3974 \simeq 16.6 \tag{21}$$

$$b \equiv \frac{P}{\rho CT} \simeq 0.3 \tag{22}$$

$$\ell \equiv \frac{L_{\text{vap}}}{CT} \simeq 1.6 \tag{23}$$

all while assuming the background particle density is small compared to the background gas density

$$\rho_{\text{par}} \ll \rho_{\text{gas}} = \rho_{\text{sat}} = \rho_{\text{tot}} \equiv \rho\,. \tag{24}$$

Figure 1 shows the eigenfrequency solutions of the cubic (18) solved numerically. All modes are unstable, growing exponentially in time. In the following subsections we analytically sketch eigenfrequencies and eigenmodes in various limits to develop physical intuition.

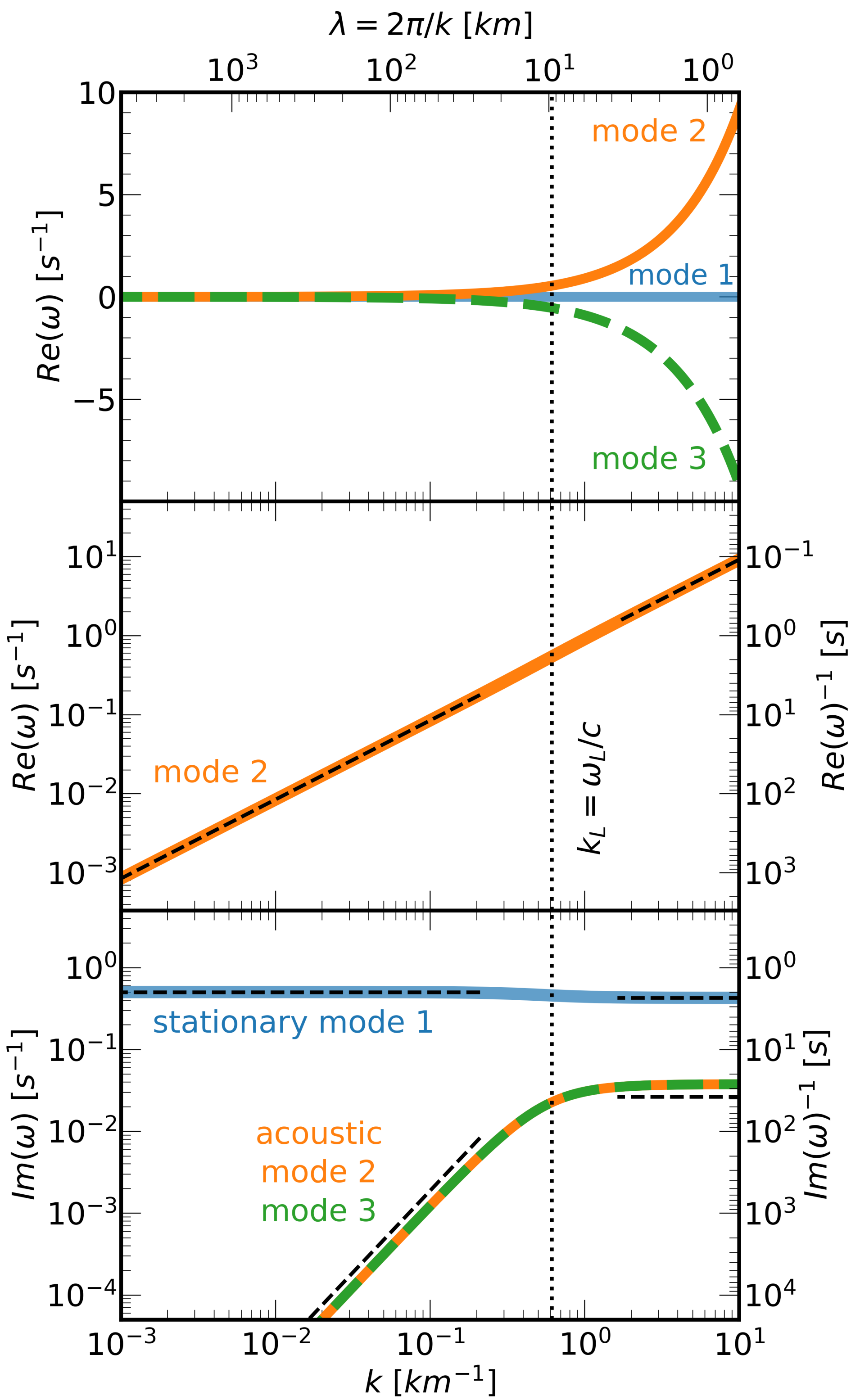

Figure 1. Eigenmode frequencies (colored curves), obtained by numerical solution of the simplified dispersion relation (18), evaluated for fiducial parameters $T = 2300$ K and $\kappa_{\rm par} = 2.5$ cm^2/g. Mode 1 is "stationary" [Re $(\omega_1) = 0$], while modes 2 and 3 are sound waves traveling in opposite directions at approximately speed $c \equiv \sqrt{P/\rho} \simeq 0.8$ km/s. All three modes grow with time [Im $(\omega) > 0$]. The dotted vertical line marks $k_{\rm L} = \omega_L/c$ dividing low-k and high-k regimes. Dashed black lines show analytic asymptotic results in those two regimes (eqs. 28, 30, and 31). Agreement with the numerical results is excellent; the analytic curves for modes 2 and 3 in the bottom panel are offset vertically from the numerical curves for clarity.

2.4.1. *Stationary mode growth rates*

The alternating real and imaginary coefficients of the cubic (18) imply that a root with $\mathrm{Re}(\omega) = 0$ and $\mathrm{Im}(\omega) > 0$ — a "stationary" (zero phase speed) growing mode — is possible. We can estimate this purely imaginary root in high-k and low-k limits. Dividing (18) by $(1 + \ell a)$, and grouping terms to highlight stationary-mode behavior, we have

$$\omega^2(\omega - i\omega_L) - c^2k^2\left(\Gamma\omega - i\frac{1+a}{a}\omega_L\right) = 0 \tag{25}$$

where

$$\omega_L \equiv \frac{a\omega_T}{1+\ell a} \simeq \frac{4\sigma T^4\kappa_{\rm par}}{L_{\rm vap}} \simeq 0.5\left(\frac{T}{2300\,\mathrm{K}}\right)^4\left(\frac{\kappa_{\rm par}}{2.5\,\mathrm{cm}^2/\mathrm{g}}\right)\,\mathrm{s}^{-1} \tag{26}$$

and

$$\Gamma \equiv \frac{(1+a)(b+\ell)}{1+\ell a} \simeq 1.2. \tag{27}$$

For $k \to 0$, we can ignore the c^2k^2 term of (25), finding $\omega = +i\omega_L$. For $k \to \infty$, we keep only the c^2k^2 term, and find nearly the same result, $\omega = +i\omega_L(1+a)/(\Gamma a)$. We see that $ck_{\rm L} \simeq \omega_L$ divides the low-k and high-k limits. To summarize,

$$\omega_1 \approx \begin{cases} +i\omega_L & k \ll \omega_L/c \\ +i\omega_L(1+a)/(\Gamma a) & k \gg \omega_L/c\,. \end{cases} \tag{28}$$

Mode 1 is stationary and growing for all k. Equation (28) is verified by the full numerical solution of (25), as shown in Figure 1. We recognize mode 1 as the radiation-condensation instability hypothesized by Chiang (2024). It amplifies over the rate at which latent heat radiates away: $\omega_L \simeq \omega_T/\ell = 4\sigma T^4\kappa_{\rm par}/L_{\rm vap}$.

2.4.2. *Acoustic mode frequencies and growth rates*

To find the other two roots of the cubic (18), we re-group terms again, this time highlighting (non-stationary) sound-wave behavior:

$$\omega(\omega^2 - \Gamma c^2k^2) - i\omega_L\left(\omega^2 - \frac{1+a}{a}c^2k^2\right) = 0. \tag{29}$$

We write $\omega = \omega_{\rm Re} + i\omega_{\rm Im}$, where the real part $\omega_{\rm Re} = O(\pm ck)$ and the imaginary part $|\omega_{\rm Im}| \ll ck$. In the high-k limit $\omega_L \ll ck$, (29) is dominated by the first term and gives $\omega_{\rm Re} \simeq \pm\sqrt{\Gamma}ck$. Now insert $\omega = \pm\sqrt{\Gamma}ck + i\omega_{\rm Im}$ back into (29), dropping $\omega_{\rm Im}^2$ and $\omega_{\rm Im}\omega_L$ terms to solve for $\omega_{\rm Im}$ to leading order. We find

$$\omega_{2,3} \simeq \pm\sqrt{\Gamma}ck + i\omega_L(\Gamma - 1 - 1/a)/(2\Gamma) \qquad k \gg \omega_L/c\,. \tag{30}$$

In this high-k limit, modes 2 and 3 are adiabatic sound waves (with adiabatic index Γ) that grow at rate $\sim 0.06\,\omega_L$. The high-k growth rate is independent of k, and slower than for the stationary mode.

We now work in the $ck \ll \omega_L$ limit. The cubic (29) is then dominated by the $i\omega_L$ term, which yields $\omega \simeq \pm[(1+a)/a]^{1/2}ck$. We insert $\omega \simeq \pm(1+1/a)^{1/2}ck + i\omega_{\rm Im}$ into (29), dropping terms of order $\omega_{\rm Im}^2$ and

$c^2k^2 \ll ck\omega_L$ to solve for $\omega_{\rm Im}$ to leading order. We find

$$\omega_{2,3} \simeq \pm(1+1/a)^{1/2}ck + \frac{i(\Gamma-1-1/a)}{2}\frac{c^2k^2}{\omega_L} \qquad k \ll \omega_L/c\,. \tag{31}$$

In this low-k limit, modes 2 and 3 are nearly isothermal sound waves that grow at rates that decrease with decreasing k. The low-k and high-k frequency behaviors for acoustic modes 2 and 3 are confirmed in Figure 1.

2.5. *Eigenvectors and work integrals*

To better understand the physical behaviors of the modes, we solve for the eigenvectors. We insert $\omega = \omega_{\rm Re} + i\omega_{\rm Im}$ into the matrix equation (17), and non-dimensionalize the state vector:

$$\begin{bmatrix} \rho(\omega_{\rm Re}+i\omega_{\rm Im}) & 0 & -\rho ck & 0 & 0 \\ 0 & \rho(\omega_{\rm Re}+i\omega_{\rm Im}) & 0 & -a\rho(\omega_{\rm Re}+i\omega_{\rm Im}) & 0 \\ 0 & 0 & c(\omega_{\rm Re}+i\omega_{\rm Im}) & 0 & -c^2k \\ \dots & \dots & \dots & \dots & \dots \\ 0 & -1 & 0 & -1 & 1 \end{bmatrix} \begin{bmatrix} \delta\rho_{\rm tot}/\rho \\ \delta\rho_{\rm gas}/\rho \\ \delta v/c \\ \delta T/T \\ \delta P/P \end{bmatrix} = \mathbf{0} \tag{32}$$

where we replaced $\rho_{\rm gas} \simeq \rho_{\rm tot}$ (background is nearly particle-free) with ρ, and omitted specifying the 4th row of the square matrix because the remaining four rows suffice to solve for the eigenvector.

2.5.1. *Stationary eigenmode behavior*

Stationary mode 1 has $\omega_{\rm Re} = 0$, $\omega_{\rm Im} = \omega_L$ at low k, and $\omega_{\rm Im} = \omega_L(1+a)/(\Gamma a)$ at high k. Without loss of generality we scale all eigenvector components to $\delta T/T$, and solve the equations in the 2nd, 5th, 3rd, and 1st rows of (32), in that order, to find the stationary mode eigenvector

$$\mathbf{E}_1 = \begin{bmatrix} \delta\rho_{\rm tot}/\rho \\ \delta\rho_{\rm gas}/\rho \\ \delta v/c \\ \delta T/T \\ \delta P/P \end{bmatrix} = \begin{bmatrix} -(ck/\omega_{\rm Im})^2(1+a) \\ a \\ -i(ck/\omega_{\rm Im})(1+a) \\ 1 \\ 1+a \end{bmatrix} \delta T/T\,. \tag{33}$$

Pressure, gas density, and temperature fluctuations are all in phase with each other, with δP and $\delta\rho_{\rm gas}$ of higher fractional amplitude than δT (by about a factor of $a \simeq 17$) because of the exponential dependence of $P_{\rm sat}$ and $\rho_{\rm sat}$ on T. Velocity fluctuations δv run ahead of pressure fluctuations δP by a phase difference of 90°. At low k, $|\delta v/c| < |\delta P/P|$, and at high k, $|\delta v/c| > |\delta P/P|$. The particle density variation

$$\frac{\delta\rho_{\rm par}}{\rho} = \frac{\delta\rho_{\rm tot} - \delta\rho_{\rm gas}}{\rho} = \left[-\left(\frac{ck}{\omega_{\rm Im}}\right)^2 \frac{1+a}{a} - 1\right]\frac{\delta\rho_{\rm gas}}{\rho} \tag{34}$$

is 180° out of phase with the gas density variation, with $|\delta\rho_{\rm par}| = |\delta\rho_{\rm gas}|$ at low k, and $|\delta\rho_{\rm par}| > |\delta\rho_{\rm gas}|$ at high k.

Scaled pictures of the stationary eigenmode are shown in Figures 2, 3, and 4. Throughout this paper, we

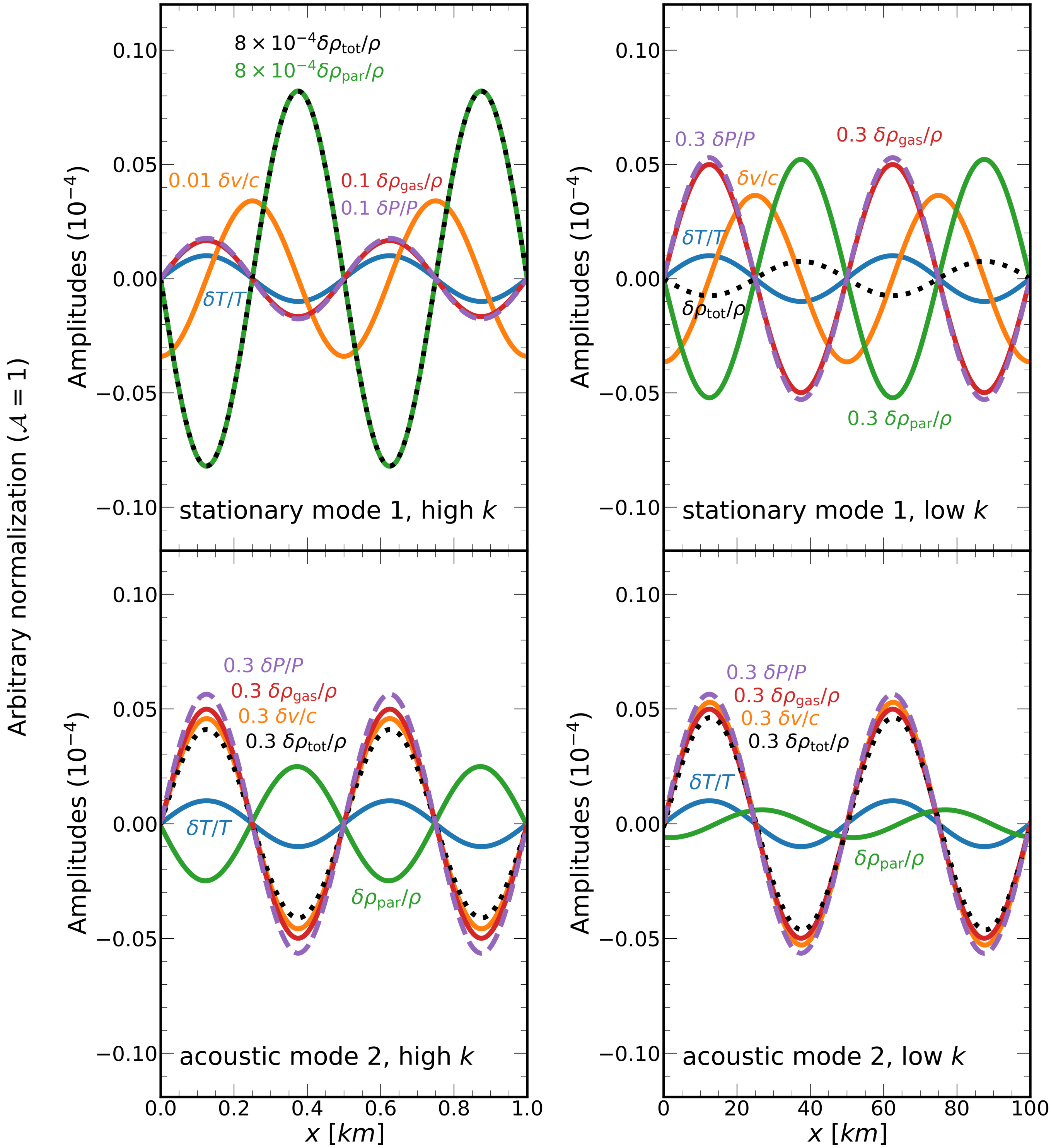

Figure 2. Eigenvector components of stationary mode 1 (having zero phase velocity; top panels), and of mode 2 which is a sound wave traveling in the positive x direction (bottom panels). Modes are sampled at high k (left) and low k (right; note the change in x-scale) relative to $k_{\rm L} = \omega_L/c \simeq 0.6\ {\rm km}^{-1}$ (wavelength $2\pi/k_{\rm L} \simeq 10$ km). In every panel, the perturbation temperature $\delta T/T$ (blue curve) is assigned the same arbitrary amplitude and phase; amplitudes and phases of other perturbed quantities follow from the eigenmode, obtained by numerical solution of (32). Note the annotated numerical coefficients, introduced so that all curves fit in a given panel. The stationary mode at high k (top left) has especially large velocities that concentrate particles especially strongly.

initialize the perturbation temperature to

$$\left.\frac{\delta T}{T}\right|_{t=0} = \mathcal{A} \cdot 10^{-6} \sin kx \tag{35}$$

where $\mathcal{A}$ is an arbitrary normalization constant, introduced for bookkeeping. Because our entire study is in the linear regime (including the numerical experiments of §3), all perturbation quantities scale with $\mathcal{A}$, at least initially. For ease of comparison between different calculations, we set $\mathcal{A} = 1$ unless indicated otherwise.

In the low-k limit (Figs. 2 and 4), fluid velocities δv and variations in total density $\delta\rho_{\rm tot}$ are negligible. Cold and hot regions cool down and heat up independently, on timescale ω_L^{-1}, before they can communicate by pressure disturbances which travel at speed c. Cold regions get colder because they condense more particles, which radiate more and cool the fluid more, in a positive feedback loop. Likewise hot regions get hotter because they have increasingly fewer particles. Changes in the local particle-to-gas ratio occur simply from local condensation and evaporation ($\delta\rho_{\rm par} \simeq -\delta\rho_{\rm gas}$).

By contrast, in the $ck \gg \omega_L$ limit (Figs. 2 and 3), hot and cold regions can communicate, and mass is transported between them. Most of the changes in total density are from the particle density changing ($|\delta\rho_{\rm par}| \gg |\delta\rho_{\rm gas}|$; eq. 34), as particles are transported out of high-pressure hot regions into low-pressure cold regions. Gas transports these particles, but gas densities do not rise in tandem with particle densities, because the gas density is throttled by saturation equilibrium; whatever gas moves with the particles into cold regions condenses into particles. In this short-wavelength limit, we have a material instability that collects increasing numbers of particles into colder, overdense clumps by excavating mass out of hotter voids.

How much of the stationary mode's behavior depends on our use of an artificial heating term $\mathcal{H}$? The heating of hot, particle-poor ($\delta\rho_{\rm par} < 0$) regions to temperatures above the background does depend on $\mathcal{H} > 0$ — on the right-hand side of the energy equation (9), heat exchange between the fluid and infinity arises from the net difference

$$Q \equiv \mathcal{H} - 4\sigma T^4 \kappa_{\rm par}\rho_{\rm par} \tag{36}$$

which is positive for $\delta\rho_{\rm par} < 0$. Conversely, in cold, particle-rich regions ($\delta\rho_{\rm par} > 0$), the difference $Q < 0$. But Q can be still be negative in such regions if $\mathcal{H} = 0$; cold, particle-rich regions would still get colder relative to their surroundings by having more particles to emit more radiation. We are therefore led to believe that a growing mode similar to (but not identical to) the one we have found should exist when $\mathcal{H} = 0$, driven by runaway cooling and condensation. We will test this assertion in §3.

2.5.2. *Acoustic eigenmode behavior*

At high k, $\omega_{\rm Re} = \pm\sqrt{\Gamma}ck$ and $\omega_{\rm Im} = (\Gamma - 1 - 1/a)\omega_L/(2\Gamma) \ll ck$. We follow the same procedure as above to solve (32) for the eigenvector:

$$ck \gg \omega_L: \quad \mathbf{E}_{2,3} = \begin{bmatrix} \delta\rho_{\rm tot}/\rho \\ \delta\rho_{\rm gas}/\rho \\ \delta v/c \\ \delta T/T \\ \delta P/P \end{bmatrix} = \begin{bmatrix} [(1+a)/\Gamma]\left[1 \mp i(\Gamma - 1 - 1/a)\Gamma^{-3/2}\omega_L/(ck)\right] \\ a \\ \pm[(1+a)/\sqrt{\Gamma}]\left[1 \mp (i/2)(\Gamma - 1 - 1/a)\Gamma^{-3/2}\omega_L/(ck)\right] \\ 1 \\ 1+a \end{bmatrix} \delta T/T\,. \tag{37}$$

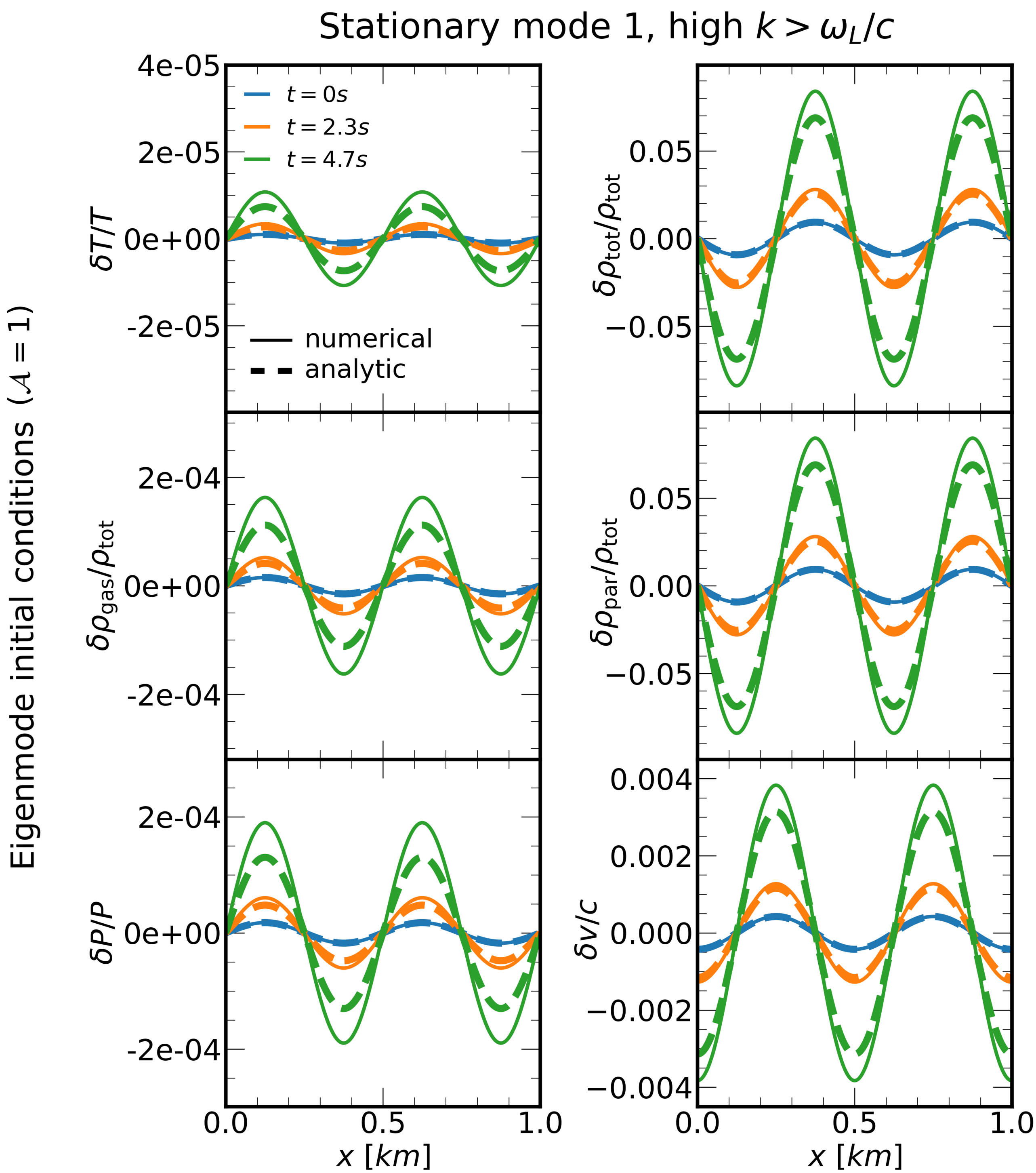

Figure 3. Time evolution of stationary mode 1 at high $k > \omega_L/c$, solved numerically using our staggered leapfrog integrator (thin solid curves, §3.1), and overlaid with analytic solutions (thick dashed curves, §2.5.1) obtained by multiplying initial values by $e^{-i\omega_1 t}$. Because the calculation is linear, all variables scale with a universal arbitrary constant $\mathcal{A}$ as defined in (35) and chosen here to be 1. The relative magnitudes of variables (e.g. $\delta\rho_{\rm par}/\rho_{\rm tot}$ vs. $\delta\rho_{\rm gas}/\rho_{\rm tot}$) are fully determined. Note how $|\delta\rho_{\rm par}| \gg |\delta\rho_{\rm gas}|$; the mode has short enough wavelength that mass can move between hot and cold regions within a condensation time ω_L^{-1}, increasing particle-to-gas ratios above what a purely condensing, static medium would yield (see Fig. 4 for an approximation of the latter). The numerical solution adopts a background particle-to-gas ratio $\rho_{\rm par}/\rho_{\rm gas} = 0.1$, and deviates from the analytic which is computed in the limit $\rho_{\rm par}/\rho_{\rm gas} \ll 1$. For better agreement, we could reduce the background $\rho_{\rm par}$ in the numerical solution, except that $\delta\rho_{\rm par}$ grows so negative for this mode that it threatens to violate mass conservation, which requires $\rho_{\rm par} + \delta\rho_{\rm par} \geq 0$.

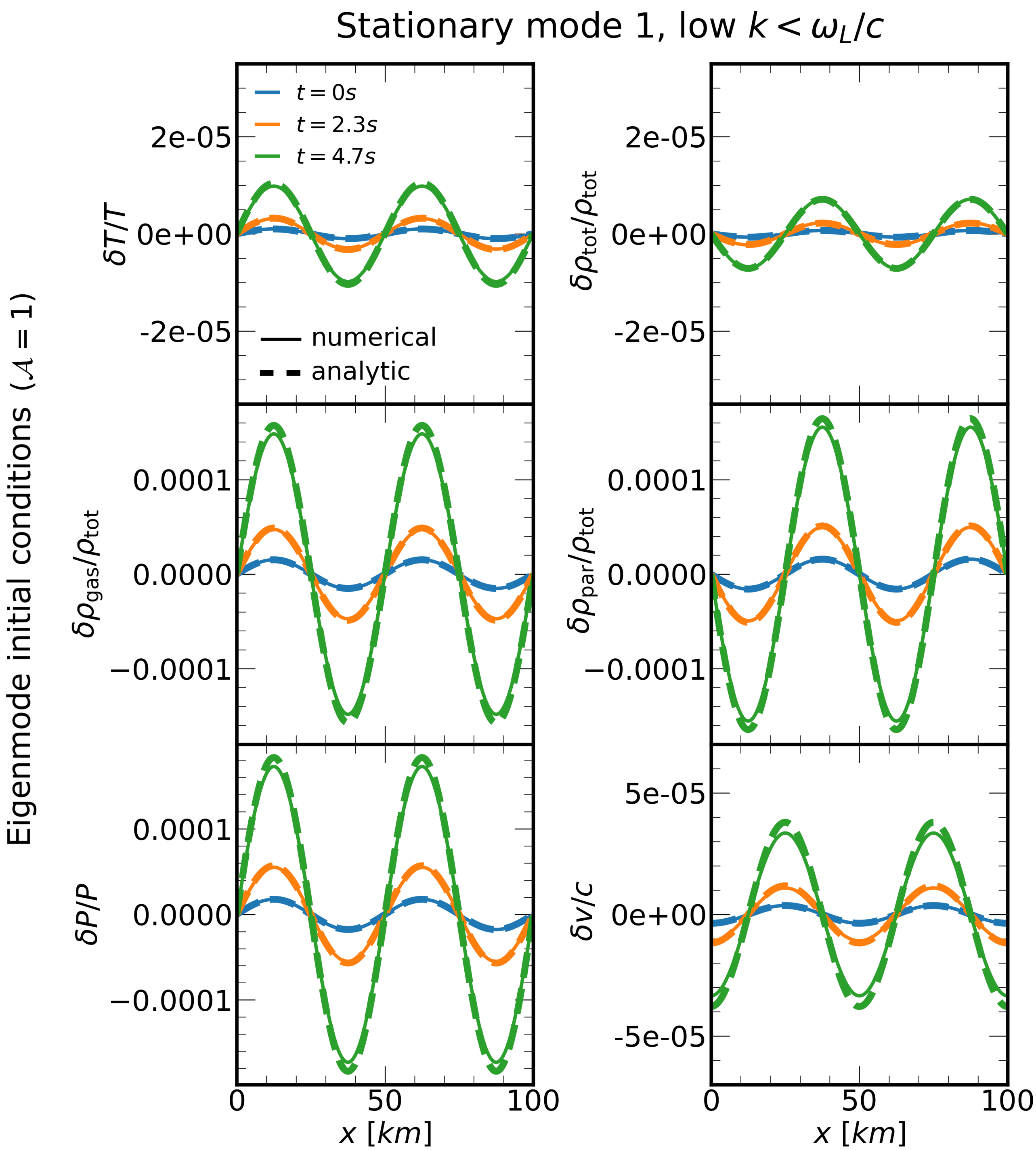

Figure 4. Same as Fig. 3, except for the stationary mode at low k. The mode has too long a wavelength for pressure gradients to transport much mass over the cooling time, and therefore gas mostly condenses without moving, with $\delta\rho_{\rm par} \simeq -\delta\rho_{\rm gas}$. As in Fig. 3, the numerical solution adopts a background particle-to-gas ratio $\rho_{\rm par}/\rho_{\rm gas} = 0.1$, whereas the analytic curves are computed in the limit $\rho_{\rm par}/\rho_{\rm gas} \ll 1$.

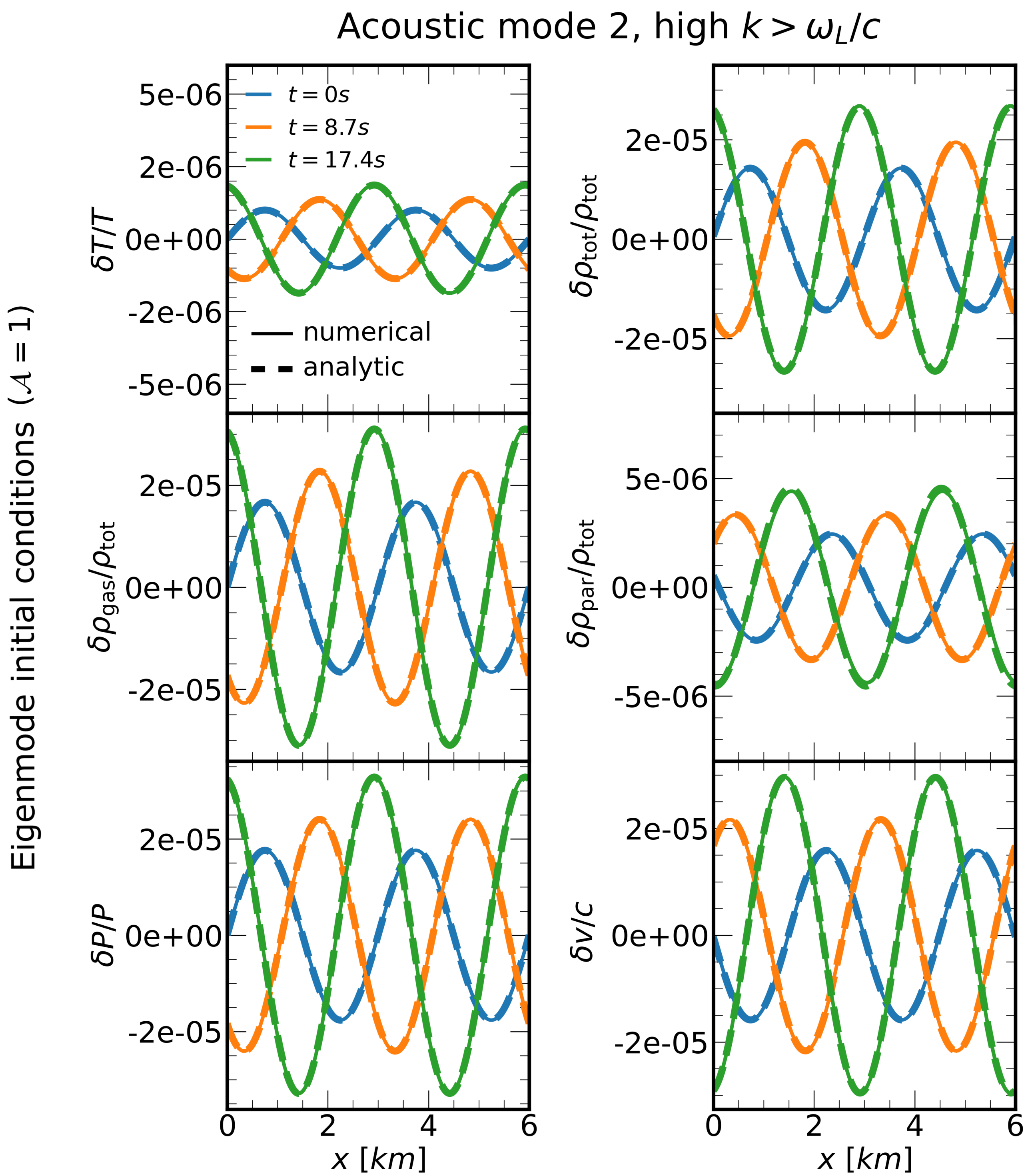

Figure 5. Time evolution of mode 2 (sound wave propagating in the positive x direction) at high k, with numerical (thin solid, §3.1) and analytic (thick dashed, §2.5.2) solutions overplotted. Mode 2 grows more slowly than mode 1; compare with Fig. 3, and note different timestamps. The numerical solution adopts a background particle-to-gas ratio $\rho_{\rm par}/\rho_{\rm gas} = 10^{-5}$, and the analytic curves are computed in the limit $\rho_{\rm par}/\rho_{\rm gas} \ll 1$.

The mode behaves like an adiabatic sound wave whose growth can be understood via the work integral (e.g. Buchler & Regev 1982):

$$+\oint P dV \propto -\oint \frac{P\, d\rho_{\rm tot}}{\rho_{\rm tot}^2} \propto -\oint \delta P \frac{\partial \delta\rho_{\rm tot}}{\partial t} dt \tag{38}$$

which measures, over one wave period, the work done by a fluid parcel of unit mass to increase the mode kinetic energy, where the parcel volume $V \propto 1/\rho_{\rm tot}$, $P = P_0 + \delta P$, and $\rho_{\rm tot} = \rho_{\rm tot,0} + \delta\rho_{\rm tot}$.[1] If $\oint PdV > 0$, the mode increases in kinetic energy, i.e., the wave amplifies. Suppose $\delta P \propto \cos(kx - \omega_{\rm Re} t)$; then from (37), $\delta\rho_{\rm tot} \propto \cos(kx - \omega_{\rm Re} t \mp \varepsilon)$ where $\varepsilon \sim \omega_L/(ck) \ll 1$ is a phase lag. Then $\partial\delta\rho_{\rm tot}/\partial t \propto \omega_{\rm Re} \sin(kx - \omega_{\rm Re} t \mp \varepsilon) \propto \pm k \sin(kx - \omega_{\rm Re} t \mp \varepsilon)$, and from (38) the work integral $\oint PdV \propto k \sin\varepsilon \propto \omega_L > 0$. Thus independent of k in this high-k limit, and regardless of the wave direction, the wave gains energy.

In more physical detail, for an oscillatory mode to gain energy every cycle period, there must be a phase lag ε such that when a fluid parcel attains an extremum in pressure (either $\max \delta P > 0$ or $\min \delta P < 0$), its volume is still changing (either expanding $\partial\delta\rho_{\rm tot}/\partial t < 0$ for $\delta P > 0$, or contracting $\partial\delta\rho_{\rm tot}/\partial t > 0$ for $\delta P < 0$). In this way positive contributions are made to the work integral (38). How does this phase lag between pressure and volume arise for our system? According to the energy eq. (9),

$$\left(P + \rho_{\rm gas} L_{\rm vap}\right) \nabla \cdot \mathbf{v} = \mathcal{H} - 4\sigma T^4 \kappa_{\rm par}\rho_{\rm par} \equiv Q \quad \text{at max or min } \delta P\,, \tag{39}$$

since $DT/Dt = 0$ when pressure reaches an extremum (pressure and temperature are always in phase on the co-existence curve; see any of the eigenvectors). We see that at $\max \delta P$, the energy to drive volume expansion ($\nabla \cdot \mathbf{v} > 0$) can come from decreasing the particle density $\rho_{\rm par}$, so that the background heating term $\mathcal{H}$ exceeds radiative cooling ($Q > 0$). Indeed, for the high-k acoustic mode, the perturbed particle density

$$\frac{\delta\rho_{\rm par}}{\rho} = \frac{\delta\rho_{\rm tot} - \delta\rho_{\rm gas}}{\rho} = \left[\frac{(1-\Gamma)a + 1}{\Gamma} \mp i \frac{(\Gamma - 1 - 1/a)(1+a)}{\Gamma^{5/2}} \frac{\omega_L}{ck}\right] \frac{\delta T}{T} \quad (ck \gg \omega_L) \tag{40}$$

is < 0 at $\max \delta T$ (in the square brackets above, the real part dominates and is < 0 for our fiducial $\Gamma \simeq 1.2$ and $a \simeq 17$). To leading order, particles evaporate as the fluid gets hotter under compression, and the consequent reduction in radiative cooling allows $\mathcal{H}$ to energize the mode at the moment of maximum pressure.

The same energy boost occurs at $\min \delta P < 0$, but for the opposite reason; now $Q < 0$ because there are more particles, causing radiative losses to dominate and the parcel to shrink ($\nabla \cdot \mathbf{v} < 0$). This cooling phase of the work cycle can occur even if $\mathcal{H} = 0$. In principle, from (39), all that is needed for a parcel to contract relative to its surroundings is for it to have more particles, which radiate more. Thus we argue that acoustic modes in a medium without background heating can still destabilize, not because they pick up more energy during the high-pressure phase of their cycle, but because they lose more energy during the low-pressure phase.

In the low-k limit, waves are quickly cooled by radiation and behave nearly isothermally:

[1] The work integral over one wave cycle cannot be evaluated for the stationary mode which has no period. Still, it is evident from (33) that a given fluid parcel in the stationary mode continuously does positive work on its surroundings: $+PdV \propto -\delta P\, \partial(\delta\rho_{\rm tot})/\partial t > 0$, whether the parcel is in a pressure peak or trough.

$$ck \ll \omega_L: \quad \mathbf{E}_{2,3} = \begin{bmatrix} \delta\rho_{\rm tot}/\rho \\ \delta\rho_{\rm gas}/\rho \\ \delta v/c \\ \delta T/T \\ \delta P/P \end{bmatrix} = \begin{bmatrix} a\left[1 \mp i(\Gamma - 1 - 1/a)(1+1/a)^{-1/2} ck/\omega_L\right] \\ a \\ \pm\sqrt{a(1+a)}\left[1 \mp (i/2)(\Gamma - 1 - 1/a)(1+1/a)^{-1/2} ck/\omega_L\right] \\ 1 \\ 1+a \end{bmatrix} \delta T/T\,. \tag{41}$$

The work integral now scales as $-\oint \delta P(\partial\delta\rho_{\rm tot}/\partial t)dt \propto k\sin[(\Gamma-1-1/a)(1+1/a)^{-1/2}ck/\omega_L] \propto k^2 > 0$, recovering the growth rate $\omega_{\rm Im} \propto k^2$. A rough description for how low-k waves amplify is that there are phase lags of order $\varepsilon \sim ck/\omega_L$ between variables that increase the mode amplitude by a fractional amount ε every wave period $1/(ck)$; then the wave e-folding time is $[1/(ck)]/\varepsilon \sim \omega_L/(c^2k^2)$.

According to the low-k eigenmode (41), $\delta\rho_{\rm par} = \delta\rho_{\rm tot} - \delta\rho_{\rm gas} = 0$ when δT is maximized ($\delta\rho_{\rm par}$ and δT are exactly $\pi/2$ out of phase according to eq. 41). This is an asymptotic result. In reality, to explain how low-k waves grow, we should have $\delta\rho_{\rm par} < 0$ (> 0) when δT is maximized (minimized). There must be a small difference between the real components of $\delta\rho_{\rm tot}$ and $\delta\rho_{\rm gas}$ that our asymptotic expressions in (41) do not capture.

3. NUMERICAL EXPERIMENTS IN LINEAR STABILITY

Here we solve the perturbation equations numerically, staying in the linear regime and in 1D, but allowing disturbances to deviate from sinusoids. The equations we solve are more primitive and general forms of the linearized perturbation equations in §2:

$$\frac{\partial\delta\rho_{\rm tot}}{\partial t} = -\rho_{\rm tot}\frac{\partial\delta v}{\partial x} \tag{42}$$

$$\frac{\partial\delta\rho_{\rm par}}{\partial t} = -\rho_{\rm tot}\frac{\partial\delta v}{\partial x} - \frac{d\rho_{\rm sat}}{dT}\frac{\partial\delta T}{\partial t} - \frac{d^2\rho_{\rm sat}}{dT^2}\frac{dT}{dt}\delta T \tag{43}$$

$$\delta\rho_{\rm gas} = \delta\rho_{\rm tot} - \delta\rho_{\rm par} \tag{44}$$

$$\frac{\partial\delta v}{\partial t} = -\frac{1}{\rho_{\rm tot}}\frac{\partial\delta P}{\partial x} \tag{45}$$

$$\begin{aligned}\rho_{\rm tot}C\frac{\partial\delta T}{\partial t} =& -C\frac{dT}{dt}\delta\rho_{\rm tot} - P\frac{\partial\delta v}{\partial x} + L_{\rm vap}\left(\frac{\partial\delta\rho_{\rm par}}{\partial t} + \rho_{\rm par}\frac{\partial\delta v}{\partial x}\right) \\ &- 4\sigma T^4\kappa_{\rm par}\,\delta\rho_{\rm par} - 16\sigma T^3\rho_{\rm par}\kappa_{\rm par}\,\delta T\end{aligned} \tag{46}$$

$$\delta P = \frac{k_{\rm B}}{\mu m_{\rm H}}(T\delta\rho_{\rm gas} + \rho_{\rm gas}\delta T)\,. \tag{47}$$

The background velocity $v = 0$, and the background total density $\rho_{\rm tot}$ = constant. Other background quantities $\rho_{\rm par}(t)$, $\rho_{\rm gas}(t)$, $P(t)$, and $T(t)$ are constant in space, and known (explicit) functions of time. While the constant background heating term $\mathcal{H}$ that we introduced in §2 does not appear explicitly in the above perturbation equations, the effects of $\mathcal{H}$ are implicit in the time evolution (or lack thereof) of background quantities. There are three cases of interest: (i) A fixed background where radiative cooling from background particles ($\rho_{\rm par} > 0$) is balanced by background heating ($\mathcal{H} > 0$; §2); (ii) A fixed background where there is neither background heating ($\mathcal{H} = 0$) nor background cooling ($\rho_{\rm par} = 0$); (iii) A time-varying background where $\mathcal{H} = 0$ and $\rho_{\rm par} > 0$ — here T will decrease secularly from unbalanced radiative cooling (hence the dT/dt terms in eqs. 43 and 46). We will consider all three cases in §3.1, §3.2, and §3.3, respectively.

As in §2, we take as small parameters $|\delta T|/T$, $|\delta P|/P$, and $|\delta\rho_{\rm gas}|/\rho_{\rm gas} \ll 1$, but do not assume $|\delta\rho_{\rm par}| \ll \rho_{\rm par}$. Unlike in §2 (cf. eqs. 13 and 13a), we retain the term $-16\sigma T^3 \rho_{\rm par}\kappa_{\rm par}\,\delta T$ in the energy equation (46) for greater accuracy.

Equations (42)–(47) are six linear partial differential equations for the six variables $\delta\rho_{\rm tot}$, $\delta\rho_{\rm par}$, $\delta\rho_{\rm gas}$, δP, δT, and δv, all functions of position x and time t. They are solved using a staggered leapfrog method (Press et al. 1992) that is 2nd order accurate in time and space, on an Eulerian grid that resolves a perturbation length scale to a fractional accuracy of $\sim 10^{-4}$, using timesteps that are typically $\sim 10^{-5}$ of the total integration duration. We have checked that our solutions have converged with grid cell size and timestep. Periodic boundary conditions are used throughout.

Bounds on $\delta\rho_{\rm par}$ and $\delta\rho_{\rm gas}$ from mass conservation (eqs. 15–16) are enforced as follows. If at a given timestep the solver's usual algorithm advances $\delta\rho_{\rm par}$ beyond its "floor" (15a), then $\delta\rho_{\rm par}$ is re-set to its floor ($-\rho_{\rm par}$), with concomitant re-settings of $\partial\delta\rho_{\rm par}/\partial t$, δT, and δP (the other variables $\delta\rho_{\rm tot}$ and δv do not need re-setting). The same flooring procedure is applied to $\delta\rho_{\rm gas}$ (15b). To check the "ceiling" condition (16a), we track in every grid cell

$$\delta\rho_{\rm par,\ phase\ change\ only} = \int^t \left[\frac{\partial\delta\rho_{\rm par}}{\partial t} - \left(\frac{\rho_{\rm par}}{\rho_{\rm tot}}\right)\frac{\partial\delta\rho_{\rm tot}}{\partial t}\right] dt \tag{48}$$

which is a running tally of particle density changes with the contribution from particle transport ($-(\rho_{\rm par}/\rho_{\rm tot})\partial\delta\rho_{\rm tot}/\partial t$) subtracted off. If (48) exceeds the ceiling value of $\rho_{\rm gas}$, then all of the background gas has condensed and the calculation is halted. An analogous check is made for the ceiling condition (16b). For the calculations shown in this paper, the ceilings are not hit, while the floors sometimes are.

3.1. *Fixed background: Eigenmode evolution ($\rho_{\rm par} > 0$ and $\mathcal{H} > 0$)*

As a first test of our numerical solver, we use it to recover the eigenmode evolution derived in §2. Accordingly, all background quantities are assumed constant; in particular $dT/dt = 0$. We adopt $T = 2300$ K, $\kappa_{\rm par} = 2.5$ cm^2/g, and $\rho_{\rm gas} = \rho_{\rm sat}(T)$. We initialize $\delta T/T$ to be the sinusoid (35) with normalization constant $\mathcal{A} = 1$. Other perturbation variables are initialized in relation to $\delta T/T$ according to the simplified matrix eq. (32).

Figures 3, 4, and 5 show the time evolution of perturbations starting from three sets of initial conditions that illustrate, respectively, a high $k > \omega_L/c$ stationary mode, a low-k stationary mode, and a high-k acoustic mode. In each case, the numerical solution compares well with the analytic solution obtained by multiplying initial values by $\exp(-i\omega t)$. Deviations between analytic and numerical solutions are due to technical differences between the calculations. The largest deviations manifest for the high-k stationary mode (Fig. 3), where the analytic solution (33) assumes the limit $\rho_{\rm par}/\rho_{\rm gas} \ll 1$ (eqs. 13a and 24), and the numerical solution adopts $\rho_{\rm par}/\rho_{\rm gas} = 0.1$. The latter choice is made to keep $\rho_{\rm par} + \delta\rho_{\rm par} \geq 0$ in the code (the floor condition 15a), since for the high-k stationary mode, $\delta\rho_{\rm par}$ can be negative and grow to especially large magnitude, requiring a commensurately large $\rho_{\rm par}$. We have verified that discrepancies between analytic and numerical solutions are eliminated by choosing $\rho_{\rm par} \ll \rho_{\rm gas}$ in the numerical solution, and $\mathcal{A} \ll 1$ to force $|\delta\rho_{\rm par}|/\rho_{\rm par} \ll 1$ at all times (data not shown). To avoid analogous discrepancies for the high-k acoustic mode (Fig. 5), we set $\rho_{\rm par}/\rho_{\rm gas} = 10^{-5}$, which we can do in this case without violating $\delta\rho_{\rm par} \geq -\rho_{\rm par}$ (even for $\mathcal{A} = 1$) because the acoustic mode grows relatively slowly.

3.2. *Fixed background: No background particles or heating ($\rho_{\rm par} = 0$ and $\mathcal{H} = 0$)*

We now experiment with a fixed background that has no particles or heating. Relative to the background $\rho_{\rm par} = 0$, the perturbation particle density $\delta\rho_{\rm par}$ can be positive from condensing background gas, but not negative since there are no background particles to evaporate (15a). This discontinuity in behavior cannot be accommodated by the Fourier analysis of §2.

Background quantities aside from $\rho_{\rm par} = 0$ are the same as those for §3.1. Initial perturbations are as follows: $\delta T/T = 10^{-6}\sin[2\pi x/(0.5\,{\rm km})]$ (i.e. $\mathcal{A} = 1$ and high $k > \omega_L/c$), $\delta v = 0$, $\delta\rho_{\rm par} = \max(0, -d\rho_{\rm sat}/dT \cdot \delta T) \geq 0$, and $\delta\rho_{\rm gas} = -\delta\rho_{\rm par}$. Our initial $\delta T/T$ is the same as that of the high-k stationary eigenmode of Fig. 3, but the other perturbation variables do not follow those of any eigenmode. For these input parameters, $\delta\rho_{\rm par}$ hits its floor of 0 and we need to apply the re-setting procedure for the first 2 timesteps of the integration, out of a total of over 40000 steps spanning 4.7 seconds. Re-setting to the floor is hardly needed because the fluid mostly cools when $\mathcal{H} = 0$, $\rho_{\rm par} = 0$ and $\delta\rho_{\rm par} \geq 0$ (see the last two terms of the energy eq. 46); eventually $\delta T < 0$ and $\delta\rho_{\rm par} > 0$ everywhere.

Figure 6 shows the time evolution of perturbed quantities for our non-eigenmode initial conditions, and can be compared against Fig. 3 for the stationary eigenmode. Qualitatively, the behaviors shown are similar: mass is transported from regions of low particle density to regions of high particle density. In both figures, the peaks in $\delta\rho_{\rm par}$ grow exponentially with similar e-folding times, but the contrast between peaks and troughs is smaller in Fig. 6: the $\delta\rho_{\rm par} < 0$ troughs of the eigenmode are flattened and made > 0 when $\rho_{\rm par} = 0$. Figure 7 traces how the peak-to-trough contrast $\max\delta\rho_{\rm par}/\min\delta\rho_{\rm par}$ decreases with time when $\rho_{\rm par} = 0$.

Unlike in the eigenmode, phase relationships between $\delta\rho_{\rm par}$, δv, and δP are not fixed. For example, in Fig. 6, $\max\delta\rho_{\rm par}$ does not always correspond to $\min\delta P$, and fluid velocities δv do not always point from high to low δP (contrast with Fig. 3).

3.3. *Time-varying background: A secularly cooling medium ($\rho_{\rm par} > 0$ and $\mathcal{H} = 0$)*

We finally experiment with a background state having a seed particle density ($\rho_{\rm par} > 0$) but no heating ($\mathcal{H} = 0$). Such a background, assumed spatially uniform and motionless, cools secularly according to eq. (9) with all $\nabla\cdot$ terms zeroed out:

$$\frac{dT}{dt} = -\frac{4\sigma T^4 \rho_{\rm par}\kappa_{\rm par}}{\rho_{\rm tot}C + L_{\rm vap}(d\rho_{\rm sat}/dT)}\,. \tag{49}$$

For a given initial temperature $T(0) = 2300$ K, initial gas density $\rho_{\rm gas}(0) = \rho_{\rm sat}(T(0))$, and initial particle-to-gas ratio $\rho_{\rm par}(0)/\rho_{\rm gas}(0)$, eq. (49) is solved as an ordinary differential equation for $T(t)$ with $\rho_{\rm par} = \rho_{\rm tot} - \rho_{\rm sat}(T)$ and $\rho_{\rm tot} = \rho_{\rm gas} + \rho_{\rm par} =$ constant. Remaining parameters are set to fiducial values ($C = 8\times10^6$ erg/g/K, $L_{\rm vap} = 3\times10^{10}$ erg/g, $\kappa_{\rm par} = 2.5$ cm^2/g). From $T(t)$ we obtain $P(t) = P_{\rm sat}(T)$ and $\rho_{\rm gas}(t) = \rho_{\rm sat}(T)$.

Figure 8 shows the time evolution of background quantities for two initial particle-to-gas ratios $\rho_{\rm par}(0)/\rho_{\rm gas}(0) = \{10^{-5}, 10^{-1}\}$. After a nearly isothermal phase when cooling is slow because particle densities are low, the temperature, pressure, and gas density drop precipitously around a time

$$t_{\rm condense} \sim \frac{L_{\rm vap}}{4\sigma T(0)^4\kappa_{\rm par}}\ln\left(\frac{\rho_{\rm tot}/2}{\rho_{\rm par}(0)}\right) \tag{50}$$

when the bulk of the background medium condenses. Equation (50) is an order-of-magnitude estimate derived as follows. For a given mass in particles to e-fold, radiation must carry away the latent heat of a gas mass comparable to the particle mass. The time for radiation to do so, $L_{\rm vap}/(4\sigma T(0)^4\kappa_{\rm par})$, is independent

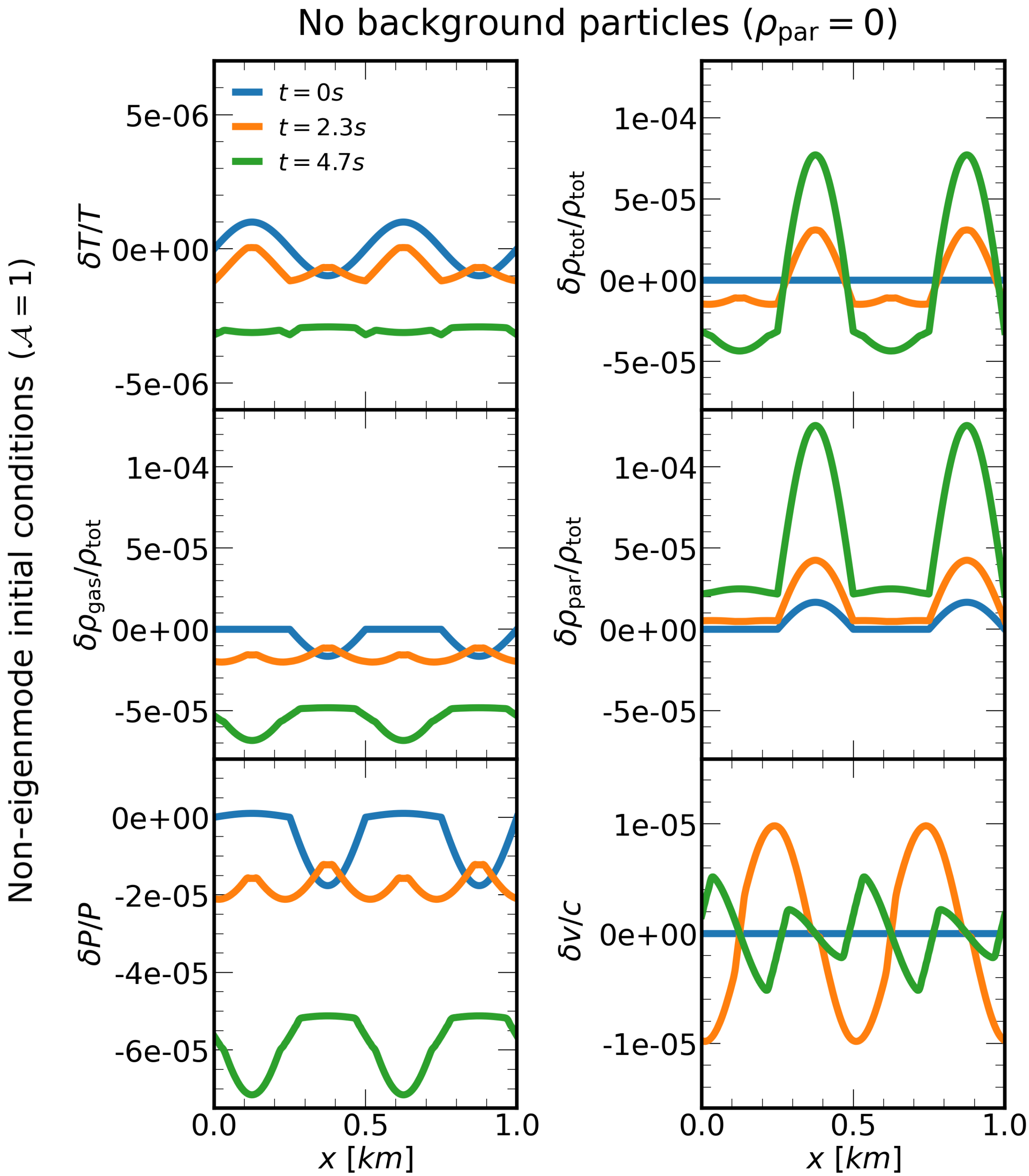

Figure 6. Time evolution of perturbations with no background particles ($\rho_{par} = 0$) and no background heating ($\mathcal{H} = 0$), calculated by numerical solution of eqs. (42)–(47) with $\delta\rho_{par} \geq 0$ enforced (§3.2). Input parameters are: $T = 2300$ K, $\rho_{gas} = \rho_{sat}(T)$, $\delta T/T = 10^{-6}\sin[2\pi x/(0.5\,\mathrm{km})]$, $\delta v = 0$, $\delta\rho_{par} = \max(0, -d\rho_{sat}/dT \cdot \delta T)$, and $\delta\rho_{gas} = -\delta\rho_{par}$. Since the gas-particle mixture can only cool radiatively with gas condensing into more particles, eventually $\delta T < 0$, $\delta\rho_{gas} < 0$, and $\delta\rho_{par} > 0$ everywhere. As in stationary eigenmode 1, fluid is transported out of initially hot into initially cold regions, amplifying local particle-to-gas ratios above what static condensation would give ($\delta\rho_{par} > -\delta\rho_{gas}$ as opposed to $\delta\rho_{par} = -\delta\rho_{gas}$). Compared to the eigenmode, however, max $\delta\rho_{par}$ grows more slowly here, and transport is not as coherent; the peaks and troughs of δP and δv change in position with passing time (contrast with Fig. 3). Consequently, the difference between particle-rich (max $\delta\rho_{par}$) and particle-poor (min $\delta\rho_{par}$) regions diminishes (see also Fig. 7).

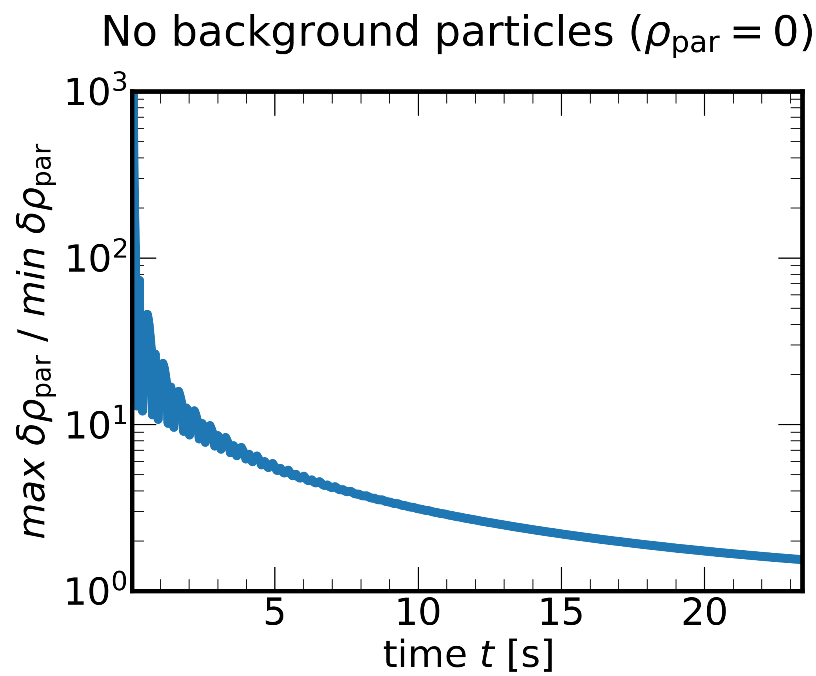

Figure 7. Time variation of the contrast between particle-rich and particle-poor regions, in the case where there are no background particles ($\rho_{\rm par} = 0$) and no background heating ($\mathcal{H} = 0$). Although both max $\delta\rho_{\rm par}$ and min $\delta\rho_{\rm par}$ grow exponentially fast (see companion Fig. 6), the difference between them diminishes, and the medium becomes increasingly uniform.

of mass or length scale under our assumption that radiation escapes freely. The logarithm in $t_{\rm condense}$ counts the number of particle mass e-foldings needed to condense half the medium, and explains why in Fig. 8 the timescale for background evolution depends only weakly on $\rho_{\rm par}(0)/\rho_{\rm gas}(0)$.

We substitute $T(t)$, $P(t)$, $\rho_{\rm gas}(t)$, and $\rho_{\rm par}(t) = \rho_{\rm tot} - \rho_{\rm gas}(t)$ into eqs. (42)-(47) and use our leapfrog integrator to solve for the evolution of small perturbations atop the time-varying background. Figure 9 shows the evolution of perturbations using the same high-k stationary eigenmode initial conditions as in Figure 3. Qualitatively, the evolutions are similar. Background quantities change by only order-unity factors over the time range plotted, and the initial perturbation is small enough that even as the mode grows, neither the floor nor ceiling on $\delta\rho_{\rm par}$ is reached. At the same time $t = 4.7$ s, $\delta\rho_{\rm par}/\rho_{\rm tot}$ is higher in Figure 9 than in Figure 3 by a factor of 2. We attribute the faster particle growth rate to the reduction in latent heating as the background gas density declines. One way to see this is to re-derive the stationary mode growth rate in the high-k limit, now taking care to distinguish between $\rho_{\rm gas}$ and $\rho_{\rm tot}$:

$$\omega_1 = \frac{+ia\omega_T}{b + \ell\rho_{\rm gas}/\rho_{\rm tot}} \,. \tag{51}$$

The factor of $\rho_{\rm gas}/\rho_{\rm tot}$ is set to unity in the less general eq. (28), and here in (51) increases ω_1 as $\rho_{\rm gas}$ decreases. Note how $\rho_{\rm gas}$ multiplies against the latent heat parameter ℓ (see also the term $\propto L_{\rm vap}\rho_{\rm gas}$ in the master energy eq. 9).

As a second experiment, we start with non-eigenmode initial conditions: $\delta T/T = 7 \times 10^{-4}\sin[2\pi x/(0.5\,{\rm km})]$ (i.e. $\mathcal{A} = 700$ and high $k > \omega_L/c$), $\delta v = 0$, $\delta\rho_{\rm par} = \max(-\rho_{\rm par}(0), d\rho_{\rm sat}/dT \cdot \delta T)$, and $\delta\rho_{\rm gas} = -\delta\rho_{\rm par}$. Background initial conditions are the same as those above except $\rho_{\rm par}(0)/\rho_{\rm gas}(0) =$

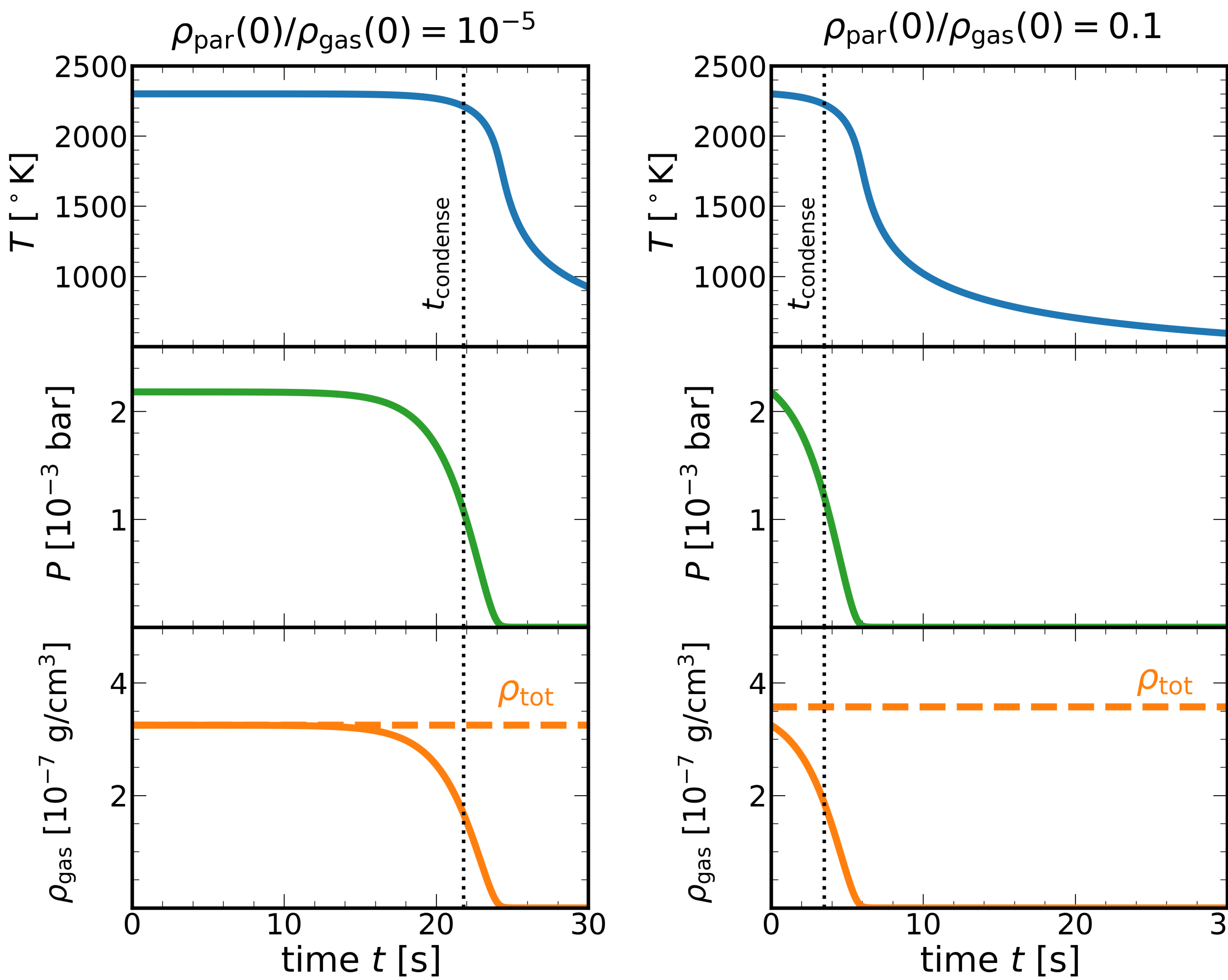

Figure 8. When there is a non-zero initial background particle density ($\rho_{\rm par}(t = 0) > 0$), but no heating ($\mathcal{H} = 0$), background quantities T, P, and $\rho_{\rm gas}$ decrease secularly as the gas-particle mixture radiatively cools, and gas condenses into particles. Dotted vertical lines mark $t_{\rm condense}$ when roughly half of the gas has condensed, as estimated by (50). This condensation time is only logarithmically sensitive to the initial particle-to-gas ratio labeled above each set of plots. In the optically thin limit, the rate of temperature decrease scales with $\rho_{\rm par}T^4$ (eq. 49), which reaches its maximum near $t_{\rm condense}$ because of increasing $\rho_{\rm par}$, and later falls because of decreasing T. Pressure and gas density under saturated conditions are exponentially sensitive to temperature and drop steeply.

10^{-2}. These inputs are similar to those of §3.2 except for the larger temperature perturbation and non-zero initial background particle density.

Figures 10 and 11 show the evolution from this non-eigenmode experiment. The initially large perturbation amplitude ($\mathcal{A} = 700$) and relatively small $\rho_{\rm par}(0)$ cause $\delta\rho_{\rm par}$ to hit the floor of $-\rho_{\rm par}$ at $t = 0$: the troughs in $\delta\rho_{\rm par}$ start flattened. Afterward, the $-\rho_{\rm par}$ floor (tracked by horizontal dashed lines in Fig. 10) becomes more negative from condensing background gas, freeing the $\delta\rho_{\rm par}$ troughs to become more negative as well (contrast with Fig. 6). Mass is transported at relatively large velocities out of particle troughs and into particle crests, and eventually at $t = 8.5$ s, the particle trough again hits the floor. The creation of a particle

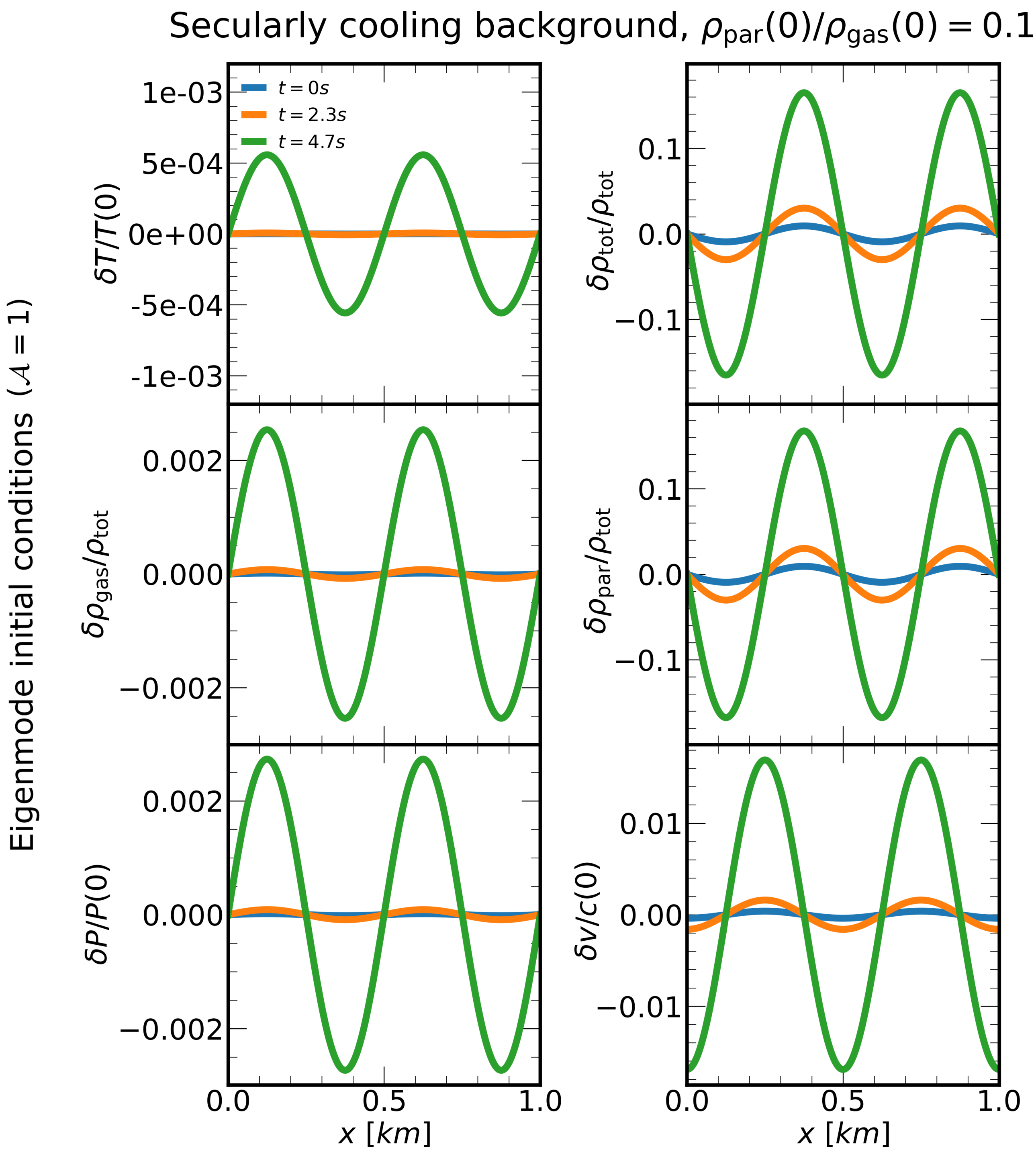

Figure 9. Numerical evolution of perturbations on top of a secularly cooling background ($\mathcal{H} = 0$, and initial particle-to-gas ratio $\rho_{par}(0)/\rho_{gas}(0) = 0.1$). See Fig. 8, right panel, for how background quantities evolve. Initial perturbations at $t = 0$ are identical to those of the high-k stationary eigenmode in Fig. 3. Comparing the results here for a time-varying background with those in Fig. 3 for a fixed background, we see that perturbations grow similarly — qualitatively the evolution is that of the high-k stationary eigenmode, with $|\delta\rho_{par}| \gg |\delta\rho_{gas}|$. Perturbations grow faster here as the background gas density ρ_{gas} decreases (eq. 51).

void ($\delta\rho_{\rm par} + \rho_{\rm par} = 0$) at this time can be seen more directly in the companion Fig. 11, which tracks the evolution of the total particle-to-gas ratio at the location of minimum $\delta\rho_{\rm par}$.

4. SUMMARY AND DISCUSSION

We have shown that a hot saturated vapor and its particle condensates are subject to a linear instability whereby particle overdensities amplify exponentially. When particles freely radiate their energy to infinity, the particle-rich get richer and the particle-poor get poorer — regions of saturated gas that are overdense in particles radiate more, thereby cooling and condensing faster. In the fastest growing mode, clumps and voids grow in place (the mode has zero phase velocity) with an e-folding time ω_L^{-1} equal to the time it takes a perturbation to radiate away its latent heat of condensation: $\omega_L^{-1} \simeq L_{\rm vap}/(4\sigma T^4 \kappa_{\rm par})$ for latent heat $L_{\rm vap}$ (energy per gas mass), Stefan-Boltzmann constant σ, temperature T, and opacity $\kappa_{\rm par}$ (cross section per particle mass). This growth time is independent of wavelength $2\pi/k$ in the radiation free-streaming limit, and measured in seconds for mm-sized particles at $T \simeq 2300$ K. Particle densities grow most dramatically if the growth time ω_L^{-1} is longer than the time it takes a sound wave traveling at speed c to cross a perturbation lengthscale. In this high $k > \omega_L/c$ regime, pressure gradients have enough time to transport mass out of high-temperature, high-pressure, particle-poor zones into low-temperature, low-pressure, particle-rich zones. For reference, a cloud of saturated silicate vapor kilometers across contains the mass equivalent of a solid planetesimal tens of meters in size.

This radiation-condensation instability is present whether or not the medium is subject to a constant background heating term $\mathcal{H}$. If $\mathcal{H} \neq 0$, then an equilibrium state can be formally defined and perturbed, leading to unstable eigenmodes. The eigenmode analysis is akin to that underlying Field's (1965) thermal instability; there as here, the dispersion relation for Fourier modes is a cubic equation for wave frequency, with two acoustic modes and a "thermal condensation" mode (analogous to our high-k, zero phase speed, fast growing mode), all of which can be unstable. If on the other hand $\mathcal{H} = 0$, then no equilibrium can be defined, as the fluid cools secularly from whatever particles are present. Perturbations on top of this time-varying background are still unstable, as we have shown by numerical experiment. Perturbations grow faster as the background gas density decreases and latent heating diminishes.

Our study assumed a wholly condensible gas, i.e. a medium composed entirely of silicates and/or metals. Adding an inert, non-condensible gas like hydrogen increases the dynamical and thermal inertia of the fluid, and would be expected to slow growth rates. Chiang (2024) found that adding H_2 to condensing, cavitating bubbles slowed their collapse. The radiation-condensation instability thus tempered might still generate overdensities large enough to trigger other concentration mechanisms, such as the streaming instability and gravitational instability (e.g. Li & Youdin 2021). Vapor plumes from colliding asteroids are practically H_2-free insofar as plume pressures overwhelm nebular pressures (Choksi et al. 2021); the latter declines to zero as the protoplanetary disk dissipates (Krot et al. 2005). Whole condensible gases — second-generation gas from vaporizing collisions between rocky/icy bodies — may also be found in extrasolar debris disks (e.g. Marino et al. 2022, and references therein).

Our linear instability depends on optically thin radiative cooling: the ability of particle overdensities to shed their energy to infinity. The nonlinear study of cavitating bubbles by Chiang (2024) found a similar requirement: although the bubbles themselves could be optically thick, their surroundings needed to have a lower radiation temperature to serve as an energy sink. To our knowledge, Field's thermal instability only manifests in environments where cooling photons can freely escape, including the solar corona (e.g. Brughmans et al. 2022), the diffuse interstellar medium (e.g. Jennings & Li 2021), and the intracluster medium in galaxy clusters (e.g. Qiu et al. 2020).

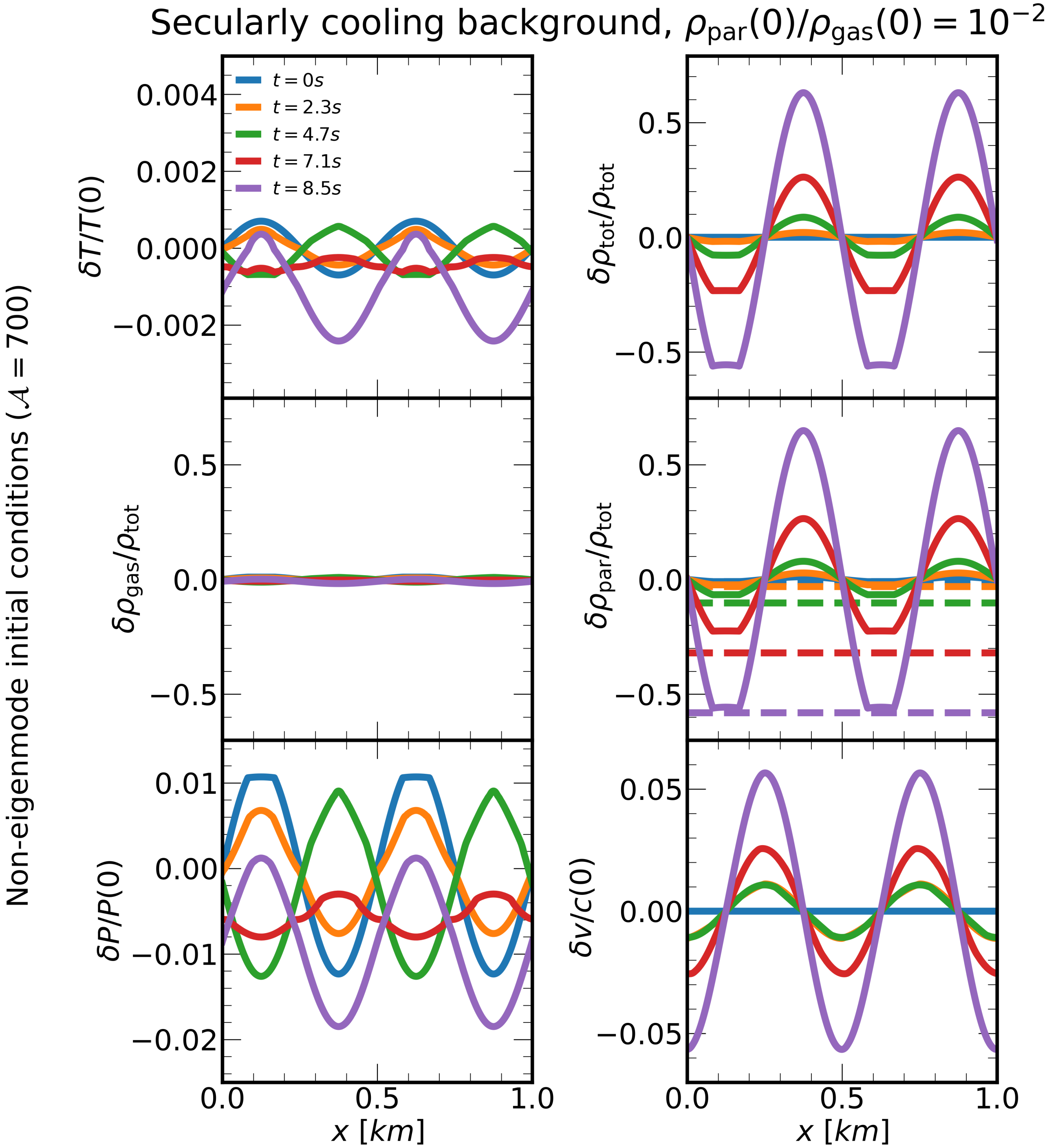

Figure 10. Another numerical experiment in perturbing a background that secularly cools ($\mathcal{H} = 0$), now with an initial background particle-to-gas ratio of $\rho_{par}(0)/\rho_{gas}(0) = 10^{-2}$, and non-eigenmode initial conditions: $\delta T/T = 7 \times 10^{-4} \sin[2\pi x/(0.5\,\mathrm{km})]$, $\delta v = 0$, $\delta\rho_{par} = \max(-\rho_{par}(0), d\rho_{sat}/dT \cdot \delta T)$, and $\delta\rho_{gas} = -\delta\rho_{par}$. Dashed horizontal lines in the middle right panel mark the $-\rho_{par}(t)/\rho_{tot}$ "floor", i.e. the lower bound on $\delta\rho_{par}/\rho_{tot}$ from mass conservation; the condition $\rho_{par} + \delta\rho_{par} \geq 0$ is enforced following a re-setting procedure. Our simulation parameters and initial conditions (in particular a relatively large initial temperature perturbation, $\mathcal{A} = 700$) are such that $\rho_{par} + \delta\rho_{par}$ hits zero in initially hot regions, at $t = 0$ and $t \simeq 8.5$ s (by which time more than half the background gas has condensed). The particle voids at the end of the simulation are carved out by relatively large velocities δv. See the companion Fig. 11.

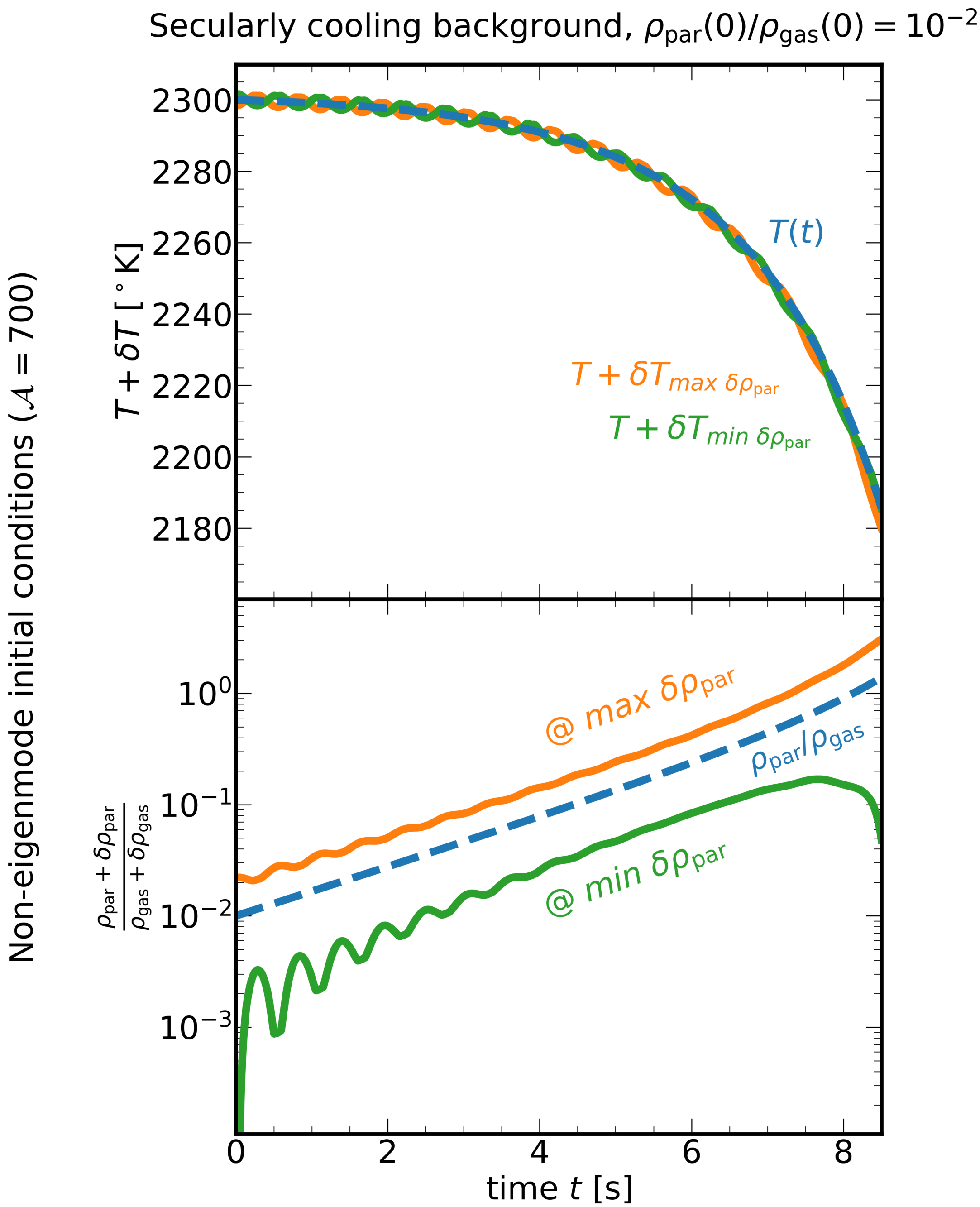

Figure 11. Evolution of temperatures and particle-to-gas ratios in the perturbed, secularly cooling fluid simulated in Fig. 10. **Upper panel:** Temperatures of the background, the location of maximum perturbed particle density (subscript max $\delta\rho_{par}$), and the location of minimum (most negative) perturbed particle density (subscript min $\delta\rho_{par}$). The location of min $\delta\rho_{par}$ varies with time and is not always half a wavelength away from the location of max $\delta\rho_{par}$ (see Fig. 10). **Lower panel:** Particle-to-gas ratios of the background $\rho_{par}(t)/\rho_{gas}(t)$, the location of maximum perturbed particle density $[(\rho_{par} + \delta\rho_{par})/(\rho_{gas} + \delta\rho_{gas})]_{\max\,\delta\rho_{par}}$, and the location of minimum perturbed particle density $[(\rho_{par} + \delta\rho_{par})/(\rho_{gas} + \delta\rho_{gas})]_{\min\,\delta\rho_{par}}$.

If instead radiative cooling is treated in the optically thick limit, with the free-streaming term $\propto -T^4\rho_{\rm par}$ in the energy equation replaced with a diffusive term $\propto \nabla \cdot (\rho_{\rm par}^{-1}\nabla T^4)$ (where $\rho_{\rm par}$ is the particle density), then instability is suppressed, as sound waves are damped by diffusion, including by thermal gas conduction (e.g. Field 1965). This presents a problem for applying thermal instability to the vapor plume from colliding asteroids, insofar as the plume may be optically thick (Choksi et al. 2021). The same problem is noted by Chiang (2024), who suggests that the radiation-condensation instability may be confined to the edges of a debris cloud, or to times when the cloud is more transparent — either early on when the cloud is too hot for many solids to condense, or later when the cloud has thinned out. Shear flows and turbulence within the impact plume may also interfere with thermal instability. These issues should be addressed in future work. See Balbus (1986) for how thermal instability plays out atop a dynamical flow, and Robertson & Goldreich (2012) for how a turbulent gas evolves upon compression or expansion.

We thank Rixin Li, Francois Tissot, J.J. Zanazzi, and Shangjia Zhang for discussions. We are also grateful to Andrew Ingersoll for reminding us of the application of thermal instability to solar prominences. This work was supported by Berkeley's Esper Larsen, Jr. fund, and a Simons Investigator grant.

Software: numpy (Harris et al. 2020), scipy (Virtanen et al. 2020), matplotlib (Hunter 2007)

REFERENCES

Balbus, S. A. 1986, ApJL, 303, L79, doi: 10.1086/184657

Bromley, J., & Chiang, E. 2023, MNRAS, 521, 5746, doi: 10.1093/mnras/stad932

Brughmans, N., Jenkins, J. M., & Keppens, R. 2022, A&A, 668, A47, doi: 10.1051/0004-6361/202244071

Buchler, J. R., & Regev, O. 1982, ApJ, 261, 301, doi: 10.1086/160341

Chiang, E. 2024, ApJL, 973, L28, doi: 10.3847/2041-8213/ad7738

Choksi, N., Chiang, E., Connolly, Harold C., J., Gainsforth, Z., & Westphal, A. J. 2021, MNRAS, 503, 3297, doi: 10.1093/mnras/stab503

Cieza, L. A., Casassus, S., Tobin, J., et al. 2016, Nature, 535, 258, doi: 10.1038/nature18612

Desch, S. J., & Connolly, H. C., J. 2002, Meteoritics and Planetary Science, 37, 183, doi: 10.1111/j.1945-5100.2002.tb01104.x

Fegley, Bruce, J., & Schaefer, L. 2012, arXiv e-prints, arXiv:1210.0270. https://arxiv.org/abs/1210.0270

Field, G. B. 1965, ApJ, 142, 531, doi: 10.1086/148317

Harris, C. R., Millman, K. J., van der Walt, S. J., et al. 2020, Nature, 585, 357, doi: 10.1038/s41586-020-2649-2

Hewins, R. H., Condie, C., Morris, M., et al. 2018, ApJL, 855, L17, doi: 10.3847/2041-8213/aab15b

Hunter, J. D. 2007, Computing In Science & Engineering, 9, 90, doi: 10.1109/MCSE.2007.55

Jennings, R. M., & Li, Y. 2021, MNRAS, 505, 5238, doi: 10.1093/mnras/stab1607

Johnson, B. C., & Melosh, H. J. 2012a, Icarus, 217, 416, doi: 10.1016/j.icarus.2011.11.020

—. 2012b, Nature, 485, 75, doi: 10.1038/nature10982

—. 2014, Icarus, 228, 347, doi: 10.1016/j.icarus.2013.10.022

Kittel, C., & Kroemer, H. 1980, Thermal Physics, 2nd edn. (W. H. Freeman)

Krot, A. N., Amelin, Y., Cassen, P., & Meibom, A. 2005, Nature, 436, 989, doi: 10.1038/nature03830

Li, R., & Youdin, A. N. 2021, ApJ, 919, 107, doi: 10.3847/1538-4357/ac0e9f

Marino, S., Cataldi, G., Jankovic, M. R., Matrà, L., & Wyatt, M. C. 2022, MNRAS, 515, 507, doi: 10.1093/mnras/stac1756

Perez-Becker, D., & Chiang, E. 2013, MNRAS, 433, 2294, doi: 10.1093/mnras/stt895

Press, W. H., Teukolsky, S. A., Vetterling, W. T., & Flannery, B. P. 1992, Numerical Recipes in Fortran 77: The Art of Scientific Computing, 2nd edn. (Cambridge: Cambridge University Press)

Pruppacher, H. R., & Klett, J. D. 2010, Microphysics of Clouds and Precipitation, 2nd edn. (Springer)

Qi, C., Öberg, K. I., Wilner, D. J., et al. 2013, Science, 341, 630, doi: 10.1126/science.1239560

Qiu, Y., Bogdanović, T., Li, Y., McDonald, M., & McNamara, B. R. 2020, Nature Astronomy, 4, 900, doi: 10.1038/s41550-020-1090-7

Robertson, B., & Goldreich, P. 2012, ApJL, 750, L31, doi: 10.1088/2041-8205/750/2/L31

Stewart, S. T., Lock, S. J., Carter, P. J., et al. 2025, arXiv e-prints, arXiv:2503.05636, doi: 10.48550/arXiv.2503.05636

Tielens, A. G. G. M. 2022, Frontiers in Astronomy and Space Sciences, 9, 908217, doi: 10.3389/fspas.2022.908217

Virtanen, P., Gommers, R., Oliphant, T. E., et al. 2020, Nature Methods, 17, 261, doi: 10.1038/s41592-019-0686-2

Visscher, C., & Fegley, Bruce, J. 2013, ApJL, 767, L12, doi: 10.1088/2041-8205/767/1/L12